UTRECHT UNIVERSITY

MASTER'S THESIS

Novel interface-engineered sodium-based nanocomposites as solid-state-electrolytes

Author:
Oscar BRANDT CORSTIUS

Supervisors:
Dr. Peter NGENE
Prof. dr. Petra DE JONGH

A thesis submitted in fulfillment of the requirements for the degree of Master of Science

in the group of

Inorganic Chemistry and Catalysis
Debye Institute for Nanomaterials Science

April 5, 2019

UTRECHT UNIVERSITY

Abstract

Faculty of Science
Debye Institute for Nanomaterials Science

Master of Science

Novel interface-engineered sodium-based nanocomposites as solid-state-electrolytes

by Oscar BRANDT CORSTIUS

To meet worldwide increasing energy demands and minimize CO_2 emissions, energy production from renewable sources such as wind and solar should be utilized on a large scale. However, these sources are intermittently harvested. Therefore, sufficient large-scale energy storage is required.

Sodium-based rechargeable batteries are attractive for large-scale energy storage due to the high worldwide abundance, low cost and suitable redox potential of sodium. Current high capacity Na-S batteries operate at 300°C because of the poor interfacial contact with the ceramic solid-state-electrolyte (SSE). Complex (boro)hydrides are proposed as SSEs but suffer from low ionic conductivity at moderate temperatures. Therefore, there is a need for improved electrolytes for applications in all-solid-state sodium-batteries.

In this work, melt infiltration of low melting point sodium salts in mesoporous Al_2O_3 and SiO_2 scaffolds is performed to enhance the conductivity by interface engineering. Using this approach, oxide-nanocomposites of $NaBH_4$, $NaNH_2$, $NaNO_2$, $NaNO_3$, $NaClO_3$ and $NaAlCl_4$ were prepared.

$NaBH_4$@Al_2O_3 and $NaNH_2$@SiO_2 composites with 130% pore filling show a thousandfold higher conductivity compared to crystalline bulk $NaBH_4$ and $NaNH_2$. The obtained conductivity at 297K was 2.7×10^{-6} for $NaBH_4$@Al_2O_3 and 3.1×10^{-7} Scm^{-1} for $NaNH_2$@SiO_2. The composites showed an activation energy of 0.46 and 0.69 eV respectively, lower than the crystalline bulk.

The origin of the conductivity enhancement is investigated. $NaBH_4$- and $NaNH_2$-oxide composites show a loss of long-range crystallinity induced by confinement in the pores. A reaction between the support surface hydroxyl groups and these sodium salts is found. In $NaBH_4$@Al_2O_3, B-O bonds, $Na_2B_{12}H_{12}$ species and mobile Na-ions are observed at the interface. The observed enhanced conductivity is attributed to these interfacial effects.

This work has investigated the melt infiltration approach to design novel sodium-based solid-state-electrolytes that show conductivity enhancement by three orders of magnitude. These materials show potential for applications in next generation all-solid-state sodium batteries.

Contents

List of Figures

List of Abbreviations

ASSB	All-solid-state battery
BET	Brunauer, Emmett and Teller
BJH	Barrett, Joyner and Halenda
CTAB	Hexadecyltrimethylammonium bromide
DRIFTS	Diffuse reflectance infrared Fourier transform spectroscopy
DSC	Differential scanning calorimetry
EIS	Electrochemical impedance spectroscopy
EV	Electric vehicle
FWHM	Full width at half maximum
LIB	Lithium-ion battery
MAS	Magic angle spinning
MCM-41	Mobil Composition of Matter no. 41
NASICON	Na super ionic conductor
NEXAFS	Near-edge X-ray absorption fine structure analysis
NMR	Nuclear magnetic resonance
PSD	Pore size distribution
RIXS	Resonant inelastic X-ray scattering
SBA-15	Santa Barbara Amorphous no. 15
SIB	Sodium-ion battery
SSE	Solid-state-electrolyte
ssNMR	Solid-state nuclear magnetic resonance
STP	Standard temperature and pressure
TGA	Thermal gravimetric analysis
TMAOH	Tetramethylammonium hydroxide
SEM	Scanning electron microscopy
XRD	X-ray diffraction

Chapter 1

Introduction

This chapter will cover an introduction to the subject of this thesis. At first, an overview of the current energy problem will be given together with some energy storage solutions. The working principle and chemistry of rechargeable batteries will be illustrated with the example of the lithium-ion battery. The challenges of this battery system are stated and motivation for sodium-ion batteries is provided. An overview of the literature on electrolyte improvements will be given. This chapter will end with the goals and approaches of this thesis.

1.1 Energy and energy storage

Throughout recent years worldwide energy consumption keeps increasing with a growing world population and their energy demands. For example in 2017 the global growth of primary energy consumption was 2.2% compared to a 1.7% annual average over the last 10 years. In this same year, the carbon emission from energy consumption increased by 1.6% globally.[1] This carbon emission overall contributes to a higher greenhouse gas effect, which should be minimized to meet the Paris agreement climate goal of keeping the global average temperature increase to well below 2°C.[2]

To meet worldwide energy demands and minimize associated growth in CO_2 emissions, renewable energy sources should be used on a larger scale. The European Union has set its target for 2030 to obtain at least 27% of its energy from renewable energy sources.[3] The biggest challenge considering renewable energy sources, such as wind energy and solar energy, is that they are intermittently harvested. Power generation relies on for example the wind to blow or the sun to shine. Furthermore, power generation may vary largely geographically or seasonally. This separation between generation and consumption of renewable power makes it an inefficient direct source of energy. To utilize renewable energy sources such as wind and solar to its full extent, sufficient energy storage is required.

Efforts are made to overcome this intermittency with different types of energy storage. For example, flywheels are used as a mechanical energy storage device, where a large mass is spun, storing energy in the rotational inertia i.e. kinetic energy of the wheel. In hydro-pumped energy storage, upon low energy demands water is pumped up to an elevated water reservoir, from which it flows back over a turbine when energy demand is high, making use

of the gravitational potential energy of the elevated water. Thermal energy storage uses heat capacity to reversibly store and release energy for example in geological substrates or phase change materials. Molecular fuels can be made with generated power, providing a wide range of chemical energy storage, such as methane production from carbon dioxide, water splitting into hydrogen and oxygen or hydrogen storage in (metal) hydride materials.

Rechargeable batteries have emerged as the most well-known example of electrochemical energy storage. Unlike some of the previously described storage mechanisms, rechargeable batteries can be used in a mobile device as they do not rely on large stationary facilities. Therefore, its applications are generally in light-weight mobile devices such as mobile phones and consumer electronics. Moreover, rechargeable batteries are of great interest for the upcoming e-mobility market and are implemented in electric vehicles (EVs).

1.2 Introduction to batteries

The most well-known example of a rechargeable battery is the lithium-ion battery (LIB), which is used in everyday mobile devices and EVs.[4] For a better understanding of the rechargeable battery working principle, the chemistry within a LIB will be illustrated. State of the art LIBs are based on the shuttling of lithium ions back and forth between the positive electrode (cathode) and the negative electrode (anode). For rechargeable batteries, this requires the reversible extraction of lithium ions from the electrodes. As a cathode material, generally, lithium transition-metal oxides, such as $LiCoO_2$, are used.[5] As an anode material, often graphite is used for its conductive properties and chemical stability. In a charged battery lithium ions are intercalated in the anode material, and when discharged intercalated in the cathode material (see Figure 1.1a). The anode and the cathode are fixed on a current collector and separated to prevent a short circuit of the electrons.

When the battery is supplying power, in the discharge process, negatively charged electrons and positively charged Li ions are released from the anode and transported towards the cathode. The schematic representative reaction of the anode can be described by $C_6Li_x \longrightarrow C_6 + xLi^+ + xe^-$. At the cathode the released Li ions are then intercalated and uptake of electrons occurs, described by $Li_{1-x}CoO_2 + xLi^+ + xe^- \longrightarrow LiCoO_2$. Here, the transition metal is partially reduced to a lower valence state upon discharging to compensate for the charge of the Li ion uptake (e.g. $Co^{4+} \longrightarrow Co^{3+}$).

The potential difference between the electrodes with intercalated Li ions gives rise to the high potential of the Li-ion battery (see Figure 1.1b). Upon charging an external potential is applied, reversing the reactions described above and turning the external electrical power back into electrochemically stored energy, ready for discharging upon later use. Enabling all these half-reactions requires the transport of electrons and Li ions. Electrons are easily transported between the electrodes provided by an external electrically

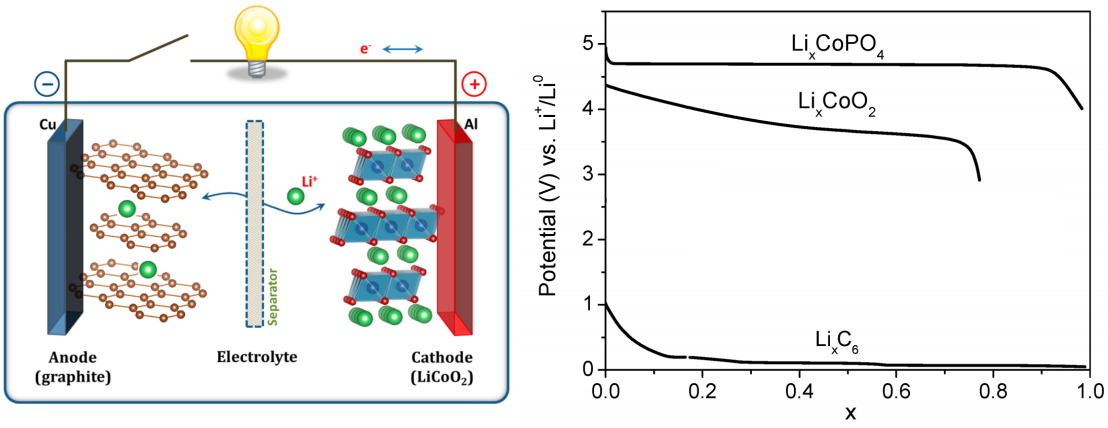

(A) (B)

FIGURE 1.1: (A) Schematic representation of a LIB. (B) Voltage profiles of metal oxide cathode and graphite anode materials at different intercalation fractions. Reproduced from Ref.[4] and Ref.[6] respectively.

conductive material. Ion transportation has to go through the so-called electrolyte. Therefore, the electrolyte should exhibit sufficiently fast ion transportation. Additionally, the electrolyte should not be electronically conductive, as short circuits between the electrodes will prevent the use of any electrical power through an external circuit, illustrated by the light bulb in Figure 1.1a. In the case of commercially available LIBs, this electrolyte is usually an organic mixture with dissolved Li-salt, such as $LiPF_6$ in an ethylene carbonate-dimethyl carbonate mixture.

1.3 Challenges in the Li-ion battery

For rechargeable battery applications on a large scale, there are several criteria that have to be met. An ideal battery of choice would be a system with reliable safety during operation and storage, low production costs, sustainable materials, ambient operating temperature, high energy density and high power density. These criteria are not met for the currently available LIB, especially regarding safety, costs and energy density, and improvement of battery design is required for large-scale applications.

One of the major problem with the LIB is the safety issues regarding the organic liquid electrolyte and has been recently critically reviewed.[7] Although these organic mixtures are generally of low cost and show high ionic conductivity ($\sim 4.5 \times 10^{-3}$ Scm^{-1} at 40°C)[8] they are also of highly flammable nature. Upon cycling in LIBs over time, dendrites of metallic lithium can accumulate on the anode. When extensive dendrite formation pierces the separator, causing a short circuit, heat generation and even fire or explosion of the flammable electrolyte could occur, referred to as thermal runaway.[7] Additional to dendrite formation, overheating, pressure buildup or cell rupture could give similar catastrophic safety issues.

Moreover, this organic liquid electrolyte is also not compatible with high energy dense electrodes. For example, the use of metallic lithium as an anode material, with the highest theoretical energy density, is not possible due to combustion upon contact with organic liquids. As a highly abundant cheap cathode material with high theoretical energy density, sulfur has been proposed. However, in an organic liquid electrolyte system the high solubility of lithium polysulfides results in a low Coulombic efficiency.[9] This is the major reason for the low energy density of the LIB ($\sim$200mAhg^{-1}) which is limited to intercalation compound electrodes, compared to for example the theoretical density of a Li-S battery (1675mAhg^{-1}).[10]

To tackle the issues associated with organic liquid electrolyte based systems, all-solid-state batteries (ASSB) are proposed as an alternative.[9] These batteries are based on a solid-state-electrolyte (SSE) material. Most SSEs provide better safety for battery electrolytes as they are generally incombustible and have larger chemical stability during battery operation. Most SSE materials have higher thermal stability compared to the liquid electrolytes, providing decreased chances of thermal runaways. Regarding energy density, the largest advantage of SSE is their compatibility with solid highly energy dense electrodes such as metallic anodes and sulfur cathodes. This increases the capacity of the battery by an order of magnitude compared to conventional battery design, such as the LIB.

Besides the chemical challenges with the LIB, there are additional economic and political challenges with the lithium-based systems in general. For example in the year 2017 lithium carbonate prices increased 37% and more than doubled in the years 2015-2017.[1] The currently known lithium resources are located for two-thirds in South-America.[1,11] Some reports have predicted that the growing production pace of lithium-based costumer devices will deplete these currently known resources in approximately 60 years from now.[12] Therefore, there is a high demand for a safe, energy dense and low-cost alternative battery chemistry for implementing in medium to high capacity batteries.

1.4 Solid-state sodium batteries

To circumvent the use of lithium-based systems, sodium-based batteries such as sodium-ion batteries (SIBs) have attracted interest due to some of its beneficial properties regarding large-scale applications such as high abundance, accessibility and suitable Na^+/Na redox potential close to Li^+/Li.[11,13–16]

With this alternative battery chemistry, the energy density of a SIB will always be lower than a LIB due to the relatively larger and heavier cation with slightly lower reduction potential. However, in the large-scale application of grid energy storage, this is not considered a critical issue, and the benefits of the low costs will be crucial. Rather than in mobile devices where light-weight materials are required, large-scale energy storage can be done in stationary facilities, where mass (and volume) are less of interest. A comparison of some important parameters for upscale energy storage is given for sodium (Na) and lithium (Li) in Table 1.1.[11,17,18].

	Na	Li
Cation radius (Å)	0.97	0.68
Atomic weight ($gmol^{-1}$)	23.0	6.9
Potential *vs.* H_2/H^+ (V)	-2.70	-3.04
Capacity metal ($mAhg^{-1}$)	1165	3829
Abundance in Earth's crust ($mgkg^{-1}$)	23.6×10^3	20
Distribution	Worldwide	70% South America
Cost carbonate (€kg^{-1})	0.5	6.5

TABLE 1.1: Comparison of sodium and lithium chemical properties and parameters regarding up-scale energy storage.

Sodium-based rechargeable batteries with energy dense electrodes, such as sodium-sulfur and sodium-nickel chloride batteries, are commercially available for over 50 years.[19,20] Their first interest emerged quickly with the discovery of fast ionic sodium conduction in the Na_2O-doped β''-alumina SSE ($11Al_2O_3{\cdot}Na_2O$).[21] However, these sodium-based-batteries require high operating temperatures of 300°C, where the electrodes are in the molten state, for sufficient interfacial contact with this particular ceramic SSE. This extreme operating temperature is not desired for use in electrochemical applications, regarding safety and energy efficiency. Therefore the development of SSE with good interfacial contact (that can well attach to or be well wetted by the electrodes) as well as sufficient room temperature conductivity, is crucial for realizing high-density sodium batteries operating at ambient temperatures.

To meet requirements for applications in ASSBs, the SSE should facilitate sufficient ion transportation while being electronically insulating. This enables the SSE to be a separator, preventing dendrite formation as well as allowing ion transportation between the electrodes. Achieving high ionic mobility is generally more difficult in solid state ionics compared to liquid organic electrolyte solutions. As a rule of thumb, the sodium-ion conductivity should be above 10^{-4} Scm^{-1}, preferably at ambient temperatures.[22] Low ionic conductivity could be problematic for the rate of charge and discharge i.e. the power density of rechargeable ASSBs. Stability over many cycles is required for efficient use of the rechargeable battery.[6]

Solid-state sodium-conductors of different types have been reported. The NASICON (Na Super Ionic CONductor) family with a chemical formula of $Na_{1+x}Zr_2Si_xP_{3-x}O_{12}$ where $0 < x < 3$, have been reported in over a thousand articles and show ionic conductivities in the range of 10^{-3} Scm^{-1} at room temperature.[14,23] However, batteries assembled with NASICON SSEs generally operate at 300°C[24], due to the poor wetting of NASICON materials with sodium anode at lower temperatures.[22] Therefore, electrolyte improvements are required for the realization of high capacity sodium-based batteries at ambient temperatures.

Sodium-based complex hydrides have recently attracted a lot of interest due to their highly conductive properties through structural modifications. For example, the sodium closo-borates $Na_2B_{12}H_{12}$, $Na_2B_{10}H_{10}$, and $NaCB_{11}H_{12}$ exhibit interesting ionic sodium conductivities in the order of

0.1, 0.01, and >0.1 Scm^{-1} above their order-disorder phase transition which occurs at 256, 87, and 107°C respectively.[25–27] However, below the phase transition, these materials still exhibit low room temperature ionic conductivity.

Recently more interest is shown towards the low-cost light-weight metal hydride and borohydride compounds as candidates for SSE, because of their practical advantages regarding processing costs and device integration.[28,29] The general problem with these SSEs is that they exhibit low room temperature conductivity. For example $NaBH_4$ and $NaNH_2$ show conductivities of 1×10^{-10} Scm^{-1} at room temperature.[30] Complex aluminum hydrides such as $NaAlH_4$ and Na_3AlH_6 have been shown to exhibit room temperature conductivities of 2.1×10^{-10} and 6.4×10^{-7} Scm^{-1} respectively.[31] Overall the room temperature conductivities of metal hydride SSEs are not satisfactory for application in ASSBs and therefore should be improved.

1.5 Electrolyte improvements

In an effort to improve the room temperature conductivity of metal hydrides, two approaches are generally applied; (1) anion substitution, where two low conductive materials are effectively combined to obtain one more conductive material and (2) interface engineering, where in close contact with a non-conductive support material, an enhancement of ionic conductivity is observed due to interfacial interactions between the salt and the support.

The approach of anion substitution has been performed on several sodium borohydride systems. For example, when mixing closo-borates with a 3:1 molar ratio of $Na_2B_{12}H_{12}$:$Na_2B_{10}H_{10}$, ionic conductivity of 3×10^{-4} at 30°C was obtained, which is approximately 2–3 orders of magnitude higher than that of either pure material.[32] The $Na_3BH_4B_{12}H_{12}$ hydroborate mixture has been reported with a room-temperature conductivity of 5×10^{-2} Scm^{-1}.[33] The promising material $Na_2(BH_4)(NH_2)$ shows sodium ionic conductivity of 2×10^{-6} Scm^{-1} at 27°C and shows an exceptional electrochemical stability of at least 6 V (*vs.* Na^+/Na).[30] In these cases, the superior conductivity arises from the formation of (highly) disordered structures in the complex mixtures with facile sodium-ion diffusion pathways.

The other approach to obtain enhanced ionic conductivity is interface engineering. An example of interface engineering on $LiBH_4$ has been shown by De Jongh et al.[34] In their work nanoconfinement via melt infiltration of $LiBH_4$ in 4.0 nm SiO_2 pores showed a thousandfold enhanced room temperature conductivity of 1×10^{-4} Scm^{-1} compared to the crystalline bulk starting material. The pristine $LiBH_4$ phase has shown to be a Li-ion conductor with high ionic conductivity only after a phase transition at 112°C, while this phase transition on no longer observed in the nanoconfined $LiBH_4$.[34,35]

Work by Choi et al. showed that a similar conductivity enhancement of $LiBH_4$ is also observed via ball milling with γ-Al_2O_3, mesoporous and amorphous SiO_2.[36,37] The enhancement is therefore ascribed to be an interfacial effect, and not ascribed to for instance stabilization of the high-temperature

phase. The interface engineering is supported by the detected B-O bondings, which are ascribed to decrease the lithium-ion hopping activation energy or enhance the mobility of the ions.[37] In literature, little to no reports on nanoconfinement have been published on sodium-based systems. The only found literature on a sodium salt nanoconfinement for conductivity enhancement has been reported as a talk abstract for sodium closo-borates.[38]

1.6 Goals and approach

This project focuses on the interfacial effect on sodium salts in oxide scaffolds. The goal of this work is to investigate the impact of interface engineering on the ionic conductivity of solid-state sodium-conductors. This approach will contribute to finding and better understanding of potential solid-state sodium-conductors for all-solid-state sodium-batteries.

As a technique for interface engineering, melt infiltration will be used as a facile synthesis technique.[39] After heating, molten sodium-salts will infiltrate into the porous support due to capillary action, if the surface energy of the molten salt is lower than the solid support, hence covering of the support lowers the total energy of the system. This covering of the support is referred to as wetting. Upon recrystallizing of the sodium salt below its melting point, composites with sodium-salt confined in the pores are obtained. Sodium-salts with low melting point will be used for practical reasons and requiring less energy input and stability of the support.

The impact of the support on the interface engineering will be tested with different supports. In this work supports with different pore size distributions (PSDs) will be used such as mesoporous γ-Al_2O_3 and SiO_2. As mesoporous silica model system Mobil Composition of Matter no. 41 (MCM-41)[40] and Santa Barbara Amorphous no. 15 (SBA-15)[41] are used. Preliminary results are obtained by tuning the support surface using aluminated SBA-15 (Al-SBA-15) in different Al/Si ratios.[42,43]

A variety of different sodium-salts are melt infiltrated in this work to investigate the effect of the different anion groups. The main focus of this work is on the light-weight metal hydride salts $NaBH_4$ and $NaNH_2$. To investigate the difference of the surface interaction between hydride and oxide-based materials, some efforts on sodium oxide salts such as $NaNO_2$, $NaNO_3$ and $NaClO_3$ were made. $NaAlCl_4$ is investigated as it is used in molten electrolyte salts at elevated temperatures.[44]

The supports and the composites are extensively studied. To investigate the wetting and infiltration during the synthesis, nitrogen physisorption and differential scanning calorimetry were performed. To determine the success of the synthesis and check the chemical stability of the sodium salts after melt infiltration X-ray diffraction and infrared spectroscopy are performed. The effect of interface engineering on the ionic conductivity is measured with electrochemical impedance spectroscopy. Nuclear magnetic resonance is performed to elucidate the interfacial interactions in $NaBH_4@Al_2O_3$ composites.

Chapter 2

Experimental details and theory

This chapter will provide all the experimental details and relevant theory behind the practical work performed in this thesis. All the chemicals used in this work will be listed and the parameters for the synthesis are stated. For all performed measurement techniques specifications of the apparatus are listed, a typical measurement is explained and a concise theory behind the technique is given.

2.1 Starting materials

The reported chemicals in this work are used as-received from the supplier without further purification. All chemicals were stored under an inert atmosphere in an Argon glovebox (H_2O and O_2 levels $<$0.1 ppm). This includes $NaBH_4$ (99.99%, trace metals basis, Sigma-Aldrich), $NaNH_2$ (98%, Sigma-Aldrich), $NaNO_3$ ($\geq$ 99.0%, reagent grade, Sigma-Aldrich), $NaNO_2$ (99.999%, trace metals basis, Sigma-Aldrich), $NaClO_3$ ($\geq$ 99.3%, ACS reagent, Fisher-Scientific), $NaAlCl_4$ (ABCR), $LiBH_4$ ($>$ 95%, Acros Organics), Al_2O_3 (Puralox SCCa-5/200, Sasol), SiO_2 (AEROSIL® 300 or 380, Evonik), Hexadecyltrimethylammonium bromide (CTAB, $\geq$ 96.0%, Sigma-Aldrich), Tetramethylammonium hydroxide (TMAOH, 25 $\%_{wt}$ in H_2O, Sigma-Aldrich), Li ribbon (99.9% trace metals basis, thickness 0.38mm, width 23mm, Sigma-Aldrich), and Sodium (ACS reagent, dry, Sigma-Aldrich).

2.2 Synthesis

2.2.1 Supports

Mesoporous ordered SiO_2 (MCM-41) was synthesized based on the procedure of Cheng et al.[45] For a single synthesis batch of MCM-41 were used: 28.82g TMAOH, 40.94g CTAB, 297.7ml deionized water and 25.00g SiO_2, for a molar ratio of 1.00 SiO_2 : 0.19 TMAOH : 0.27 CTAB : 40 H_2O. The CTAB was dissolved in the water and the TMAOH was added to the mixture while stirring at 30°C until the solution became clear. The SiO_2 was added and left stirring for 120 minutes. The mixture was aged without stirring for 24 hours isothermally. The obtained gel mixture was reacted in a Teflon-line stainless steel autoclave for 40 hours in a 140°C preheated oven. The product was filtered and washed with approximately 3 liters of deionized water to remove

any leftover surfactants. The wet product was dried in static air at 120°C for 8 hours. The dried product was heated with 1.5°Cmin^{-1} to 550°C and calcined for 12 hours.

Another mesoporous SiO_2 scaffold (SBA-15) and aluminated SBA-15 were synthesized based on the procedure of Lee et al. and Baca et al.[42,43] SBA-15 was typically synthesized by dissolving 23.4g Pluronic P123 in deionized water with 35% hydrochloric acid in a 1:26:6.25 mass ratio. The solutions were reacted in a water bath set to 45 or 55°C under strong stirring for over 3 hours. Afterwards, a silica source of 50g of tetraethyl orthosilicate was added to the solution at 500 rpm stirring and mixed for 5 minutes, before aging the mixture without stirring for 24 hours at their respective temperatures. The batches were further reacted for 24 hours in a 100°C oven. The block copolymer template was removed by extraction of 37% HCl and ethanol (90%$_{volume}$) for 1 hour before calcining at 550°C for 3 hours.

Aluminated SBA-15 supports were prepared with a Si/Al ratio of 20/1 and 10/1, further referred to as Al-SBA-15(20) and Al-SBA-15(10). This ratio was achieved by adding proportionate amounts of aluminum isopropoxide dissolved in anhydrous isopropanol or cyclohexane to dried (2h, 450°C) SBA-15 and left stirring overnight. The suspension was washed with its corresponding anhydrous solvent before calcining at 500°C for 4 hours.

Before storage and use, all supports were dried under nitrogen flow. The powders were heated with 5°Cmin^{-1} to 300°C and dried for at least 4 hours before cooling down to room temperature. All supports were stored in an Argon glovebox (H_2O and O_2 levels $<$0.1 ppm).

2.2.2 Melt infiltration

To obtain interface engineered sodium salt-oxide composites melt infiltration is used. For this approach of composite preparation, good wetting of the molten salt on the pore walls is required for sufficient infiltration into the pores. This wetting of the material is related directly to the surface energy of the salts and supports. The surface energies of amorphous γ-Al_2O_3 and SiO_2 are reported 1.52 and 0.259 Jm^{-2} respectively.[46,47] The large difference in surface energy can be explained by the large density difference of surface hydroxyl groups, which are approximately 10 and 2 OH per nm^2 for Al_2O_3 and SiO_2.[48,49] For most sodium salts, unfortunately, no surface energies are found in the literature. For $NaBH_4$ the surface energy is reported between 0.24 and 1.89 Jm^{-2}.[50]

In all melt infiltration syntheses, desired amounts of as-received sodium salts and dried supports were mixed and ground thoroughly with a pestle and mortar. The amount of sodium salt added to the mixture was based on the total pore volume measured by nitrogen physisorption. Melt infiltration of sodium salts with melting temperatures below 300°C was performed in autoclaves with pressure indicators, held airtight by a Teflon O-ring. This includes $NaNH_2$, $NaNO_2$, $NaNO_3$, $NaClO_3$ and $NaAlCl_4$ with melting temperatures of 210, 271, 308, 248 and 185°C respectively.

For $NaNH_2$-oxide composite synthesis, 8 bar NH_3 pressure was applied prior to heating. The aim of the ammonia pressure is to suppress decomposition of the salt, as NH_3 is the main decomposition product between 200 and 380°C.[51] The mixtures were heated to 225°C with 2.5°Cmin^{-1} ramp and dwelled for 15 minutes before cooling down to room temperature.

In the case of the oxide salts ($NaNO_2$, $NaNO_3$ and $NaClO_3$) 5 bar of O_2 pressure was applied prior to heating to 290, 325 and 265°C respectively. All oxide samples were heated with a 2-2.5°Cmin^{-1} ramp and dwelled at the maximum temperature for 30 minutes before cooling down to room temperature. $NaAlCl_4$ melt infiltration was performed under 10 bar Ar pressure and heated to 200°C with similar heating ramp and dwell time.

At temperatures above 300°C, the Teflon O-ring in previously described autoclave melts and the autoclave would not remain airtight. $NaBH_4$ (T_m = 500°C) melt infiltration was therefore performed in stainless steel reactors (see Figure A.1). Hydrogen pressure to suppress the $NaBH_4$ decomposition was generated in these closed reactors (∼22ml) by ∼0.1g of a $LiBH_4$-SiO_2 physical mixture, which has been shown to irreversible release hydrogen at 200°C.[52]. As a SiO_2 source MCM-41 or SBA-15 were used in a 1:1 mass ratio with the $LiBH_4$. The ground $NaBH_4$-oxide mixtures were placed in aluminum oxide cylindrical holders. The tightly closed stainless steel reactors were heated with 1.5°Cmin^{-1} to 525°C, held for 30 minutes and left to cool down to room temperature. An overview of synthesized samples in this thesis is provided in Table A.1 and A.2

2.3 Characterisation and measurements

2.3.1 Nitrogen physisorption

Nitrogen physisorption measurements are performed on the Micromeritics TriStar Surface Area and Porosity Analyzer. As samples were dried before storage, as described in Section 2.2.1, no further drying was performed prior to measurements. Sample preparation was performed in Argon glovebox and transferred to the Analyzer shortly before the measurement in an airtight glass physisorption tube. In a typical measurement between 0.02g and 0.2g of sample was measured. Measurement temperatures were carried out at 77K cooled by liquid nitrogen.

In nitrogen physisorption, the sample containing tube is degassed to vacuum before the experiment. Step-by-step a small amount of nitrogen is introduced into the tube and adsorbs onto the sample. By comparing the amount of introduced nitrogen and the relative nitrogen pressure (p/p_0, where p and p_0 are the equilibrium and saturation pressure of nitrogen at 77K) the volume of adsorbed nitrogen can be calculated. Similar steps can be performed in the desorption process, yielding a desorption isotherm curve. Although these measurements are performed at below atmospheric pressures and low temperature, the measured volumes will be converted to standard temperature and pressure (STP, T=273.15K and p=1 bar). This STP is used in the practical environment of the synthesis.

Analysis of the adsorption and desorption curves is performed with the Brunauer, Emmett and Teller[53] (BET) theory for surface area calculations and Barrett, Joyner and Halenda[54] (BJH) theory for pore size distribution analysis. The total pore volume, close to $p/p_0 = 1$, will be used for the melt infiltration pore volume calculations.

2.3.2 X-ray diffraction

Room temperature powder X-ray diffraction (XRD) measurements are carried out on a Bruker-AXS D8 Advance powder X-ray diffractometer, in Bragg-Brentano mode, equipped with automatic divergence slit and a PSD Våntec-1 detector. The radiation used is Cobalt $K_{\alpha 1,2}$ ($\lambda = 1.79026$Å) operated at 30 kV and 45 mA. The diffractometer is equipped with a primary Soller slit (2.5°), automatic divergence slit (0.6mm, 0.3°), anti-scatter slit (2.44mm), detection slit (3.54mm), PSD angle 1° and operates at a 217.5 mm $\theta - \theta$ range.

XRD sample preparation is performed an Argon glovebox. A smooth layer of powder is placed on the sample holder and transferred to the diffractometer in a customized Bruker airtight specimen holder to keep the sample under an inert atmosphere. Typical measurements were performed with 0.1° (2θ) step sizes, with 1-3 seconds step time. XRD reference patterns were obtained from the PDF-4+ 2018 database, International Centre for Diffraction Data, version 4.1801. Measured samples were not reused for other characterisation techniques.

In XRD the structure of a material is probed by the elastic scattering of monochromatic X-rays. The X-rays penetrate into the sample and diffract of the electron density (i.e. the atoms) in the sample. When the path length difference between two lattices (repetitive row or plane of aligned atoms in a crystalline material) matches exactly an integer, n, amount of times the wavelength of the incident beam, constructive interference is observed. This is described by Bragg's law: $2dsin\theta = n\lambda$, where d is the lattice spacing, θ is the incident angle and λ is the incident wavelength. The diffraction pattern measured in XRD arises from different incident angles that coherently interfere with different lattice spacings from the crystal structure.

2.3.3 Infrared spectroscopy

Diffuse reflectance infrared Fourier transform spectroscopy (DRIFTS) measurements were performed on a Perkin Elmer IR, equipped with a liquid-nitrogen cooled MCT detector. Infrared spectra were collected between 500 and 4500 cm^{-1} with a 4 cm^{-1} resolution and averaged over 16 scans. Prior to all spectra, anhydrous KBr was measured as a background. Sample preparation was performed in an Argon glovebox. A 40μl aluminum hermetic TGA sample holder pan from Perkin Elmer was filled with the sample powder and placed in a home-build airtight sample holder before transporting to the spectrometer.

In DRIFTS an infrared beam is focused on the sample material and reflectance is measured, as the light scatters off the particles. This reflective

nature makes it a useful technique for non-transparent materials. When the energy of the incoming beam matches the vibrational energy of a chemical bond, absorption of the radiation occurs. After interaction with the sample, the light that is scattered out of the material is focused by concave mirrors to the detector. This detector records the difference between the incoming beam and the altered observed IR beam and an absorption spectrum is generated.

Unless otherwise stated, obtained absorption spectra are converted to Kubelka-Munk (KM) plots using the formula: $\frac{k}{s} = \frac{(1-R)^2}{2R}$, where k, s and R are absorption coefficient, scattering coefficient and reflectance respectively.[55] The scattering coefficient is dominated by the particle size so considered constant when varying the wavelength during measurements. Spectra with higher resolution are obtained in this way, although it is based on some assumptions regarding surface roughness, uniform distribution, and absorption coefficients. Therefore only qualitative analysis can be performed. For further reading on the KM formula derivation and validity of the assumptions, the reader is referred to Ref.[56].

2.3.4 Electron microscopy

Scanning electron microscopy (SEM) images were obtained on a Thermo Fisher FEI XL30 SFEG instrument operating at an acceleration voltage of 5 kV measuring secondary electrons on a Through-Lens-Detector. Samples were sputter-coated with about 8 nm of Pt before loading into the SEM instrument.

In SEM, low-energy electrons are bombarded on the to be investigated material in an applied vacuum. The electrons penetrate the sample and after a cascade of scattering events, some back-scattered electrons escape the surface. The amount of back-scattered electrons is measured with a detector, and is dependent on, among other parameters, the sample density and morphology. Typically, the electron beam is focused and scanned over the surface using electromagnetic lenses to obtain information about the spatial distribution of electron density over the surface of the sample.

2.3.5 Differential scanning calorimetry

Differential scanning calorimetry (DSC) measurements were performed on an HP DSC 1, MultiSTAR from Mettler Toledo, equipped with an FRS5 sensor. All measurements are performed under 5 bar hydrogen pressure with a 10ml/min flow rate through the system. Prior to the measurements, the system was calibrated with In and Zn under the same hydrogen flow.

Between 5-11mg of sample was placed in a 40μl aluminum hermetic TGA sample holder pan from Perkin Elmer with a punched hole in the lid to allow gas exchange and prevent expansion and deformation of the pan upon heating. As a reference, an empty pan was used in all experiments. After sample insertion, the system was flushed two times to vacuum and filled with 3.7 bar Argon before flushing to 5.0 bar Hydrogen. The measurements were performed between 30°C and 550°C with a ramp of 10°Cmin^{-1} in the

temperature region of interest. After a heating step, the system was equilibrated for 2 minutes before cooling down, where a 5-minute isotherm after each cycle was applied.

In DSC, the heat flow measured while varying the temperature. With this technique endothermic and exothermic transition such as phase changes, decomposition, desorption, adsorption, melting and crystallization can be observed. Incorporation of compounds into small pores have been shown to exhibit different behaviours such as melting point depression or loss of crystallinity, that can be measured with this technique.[39].

2.3.6 Electrochemical impedance spectroscopy

Electrochemical Impedance Spectroscopy (EIS) measurements are performed on pressed powder pellets using a Princeton Applied Research Parstat 2273 potentiostat in a custom made measurement cell in a Büchi B-585 glass oven. The preparation and the measurements are performed in an Argon glovebox.

The measured pellets are prepared in as a symmetrical cell of electrolyte powder pressed between two pieces of either lithium foil or sodium foil. The latter has the obvious preference when working with sodium-based salts. However, in part of this project commercially available lithium foil was used (Sigma-Aldrich, 0.38mm thick) due to practical issues with obtaining reproducible sodium foil electrodes. In the last part of this project more consistently sodium foil could be produced, and measurements of interest were reproduced.

Before use, the metal foils were carefully scraped to remove any traces of metal oxide on the surface. Circles of 12mm diameter were cut out and placed in the middle of two stainless steel pellets, 13mm in diameter. Inside a die body, between 0.15g and 0.25g of composite or pure salt is pressed between two pellets, such that the sample is in good contact with the metal foil. Using a 13mm die plunger and airtight holder, the pellets were pressed to 2.0 metric tonnes of pressure. From the applied pressure and known pellet area, this pressure is calculated as $150.7 \times 10^3 \mathrm{ton/m^2}$ or 0.148 GPa. This preparation resulted in pellet thickness between 1.0 and 1.5mm after subtraction of stainless steel die thickness (12.68mm) and metal foil thickness (0.6mm for lithium and $\sim$0.1mm for sodium pressed to 2 tonnes).

In a typical EIS measurement, a 20mV rms modulated alternating current potential with frequencies from 1 MHz to 1 Hz (in 120 logarithmically displaced steps) was applied to the compressed sample. The samples were heated from room temperature with $5^\circ\mathrm{Cmin}^{-1}$ to 80°C or 130°C in steps of 10°C and allowed to equilibrate for 45 min before the measurement. Upon cooling the samples were measured in steps of 20°C, each measurement after 118 minutes of equilibration. At least two cycles were performed to investigate any instabilities of the sample upon cycling.

Impedance refers to frequency-dependent resistance, where at different applied frequencies of the alternating current potential, different resistance responses will be observed. The potentiostat measures the current as well as the phase shift, with respect to the potential, at each frequency. A large

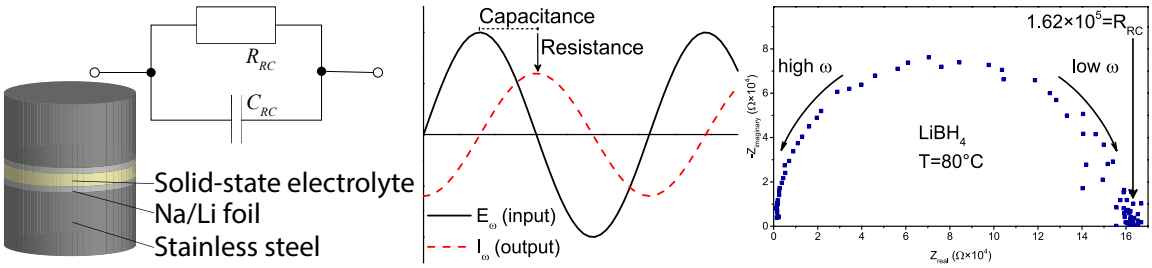

(A) (B) (C)

FIGURE 2.1: (A) Schematic representation of a pellet measured with EIS and an RC circuit consisting of a parallel resistor and capacitor. (B) Example of impedance with phase shift and amplitude decrease. (C) Complex impedance plot of $LiBH_4$ at 80°C.

resistance through an Ohmic material decreases the measured current with Ohm's law, $I = V/R$, where I, V and R, are current, potential and resistance respectively. The phase shift is typically measured between 90° and 0° from completely out of phase at high frequencies to a resonance of current and potential at lower frequencies. Impedance, Z_w, is then formulated by: $Z_w = \frac{E_0 sin(\omega t)}{I_0 sin(\omega t + \phi)} = Z_0(cos\phi + isin\phi)$, where Z_w is described by a real part cosinus (resistance) and a imaginary (capacitance) part sinus wave (see Figure 2.1b). In a Nyquist plot (see Figure 2.1c) the real and imaginary parts are plotted for each data point, and in the perfect case form a semi-circle. The Z_{real} intersection of this semicircle is the total resistance of the material.[57]

In most cases, a single component semi-circle was observed in the Nyquist plots. The data were fitted using an RC circuit, consisting of a resistance and a constant phase element (CPE) (see Figure 2.1a). The intersection of the fitted semicircle with the real impedance (Z_{real}) axis was assumed to represent the electrolyte resistance R only. Conductivity is calculated from this resistance via $\sigma = h/AR$, where σ, A, h are the conductivity, the area of the pellet, and thickness of the compressed electrolyte respectively.

2.3.7 Nuclear magnetic resonance

Solid-state nuclear magnetic resonance (NMR) measurement are performed on a Bruker 400MHz wide bore (10cm), ultra shielded 9.4 T magnet using Console AvanceIII hardware. Samples were measured in a 3.2mm magic angle spinning (MAS) zirconia rotors with vespel caps with an HXY probe. The ^{23}Na spectra were ^{1}H decoupled with 70kHz radio-frequency. For ^{23}Na measurements the reference was set to solid NaCl. For ^{11}B the pure $NaBH_4$ peak was set to -42.0ppm, according to literature, using $EtOBF_3$ as a reference.[58]

Sample preparation consisted of filling and closing of the rotor in an Argon-filled glovebox. The rotors were transferred in an inert atmosphere up to just before the measurement. The samples were measured either spinning

or without spinning (static) on the ^{1}H, ^{11}B, and ^{23}Na nuclei at room temperature. Temperature-dependent measurements were performed on ^{23}Na spectra between 263K and 353K.
High-resolution NMR measurements are performed on a Bruker 950MHz small bore (5cm), ultra shielded 22.3 T magnet using Console AvanceIII hardware. Samples were measured in a 1.3mm MAS rotor with an HXY high spinning probe. The spectra were measured at 60kHz MAS, resulting in sample temperature of $\sim$50°C. ^{1}H measurements were performed with a 90° pulse in Hahn echo mode. ^{11}B and ^{23}Na spectra were obtained with a 30° single pulse. ^{11}B spectra were ^{1}H decoupled with 16kHz radio frequency.

The NMR technique can be performed only on nuclei with an intrinsic magnetic moment and angular momentum i.e. an odd number of protons and/or neutrons. A large magnetic field is applied to sufficiently align nuclei spins in the spin up or spin down state, instead of randomly oriented in all direction. The slight difference in energy between these spin states can be measured with radio-frequency spectroscopy. When the radio-frequency photon matches this exact energy difference and is absorbed, resonance is observed. This resonance is environment dependent and hence local chemical information can be obtained from the technique.

Chapter 3

Results and discussion

In this chapter, the relevant results obtained in this thesis will be discussed. Firstly the structural characterisation of the supports and composites will be discussed, using nitrogen physisorption, SEM, XRD and DRIFTS. The investigation of the conductivity of the materials will be interpreted in detail with EIS. Lastly, an investigation into the origin of conductivity enhancement by interface engineering will be given by NMR.

3.1 Structural characterisation

3.1.1 Oxide supports

To investigate the pore size distribution (PSD), BET surface area and pore volumes of the dried oxide supports, nitrogen physisorption analysis was performed. A comparison of the PSDs is given in Figure 3.1. Each symbol represents a data point derived from BJH theory in the desorption branch. The solid lines are Gaussian fits through the data. The pore size was determined from the maximum of the Gaussian fits. The distribution of the pore width is described from the full width at half maximum (FWHM) of the Gaussian fit. BET theory was used to determine the surface area from the linear $\frac{1}{Q(p/p_0-1)}$ behaviour (where Q is the amount of nitrogen absorbed) in the $p/p_0 = 0.07 - 0.2$ nm range of the adsorption branch. The total pore volume of the support is taken from the pore volume of a single point at STP close to $p/p_0 = 1$. Overview of the physisorption analysis is given in Table 3.1.

From these results, it is seen that the synthesis of MCM-41 was successful, as particles with small pores, narrow PSD, high surface area and high pore volume are obtained. These results are in line with expectations from literature.[45] For the (aluminated) SBA-15 supports a slight pore size decrease is observed with higher alumina loading, as was expected from the synthesis when more material is grafted inside the pores of SBA-15.[43] Al-SBA-15(10) showed an increase in surface area and pore volume compared to pristine SBA-15. This is unexpected as the PSD does not seem to have changed significantly and hence is ascribed to a normalization error, where the mass of the support was underestimated. Al_2O_3 showed the largest pores, widest PSD and lowest total pore volume and BET surface area. These results confirm the mesoporosity of the oxide supports with high pore volumes, that will be used for melt infiltration.

Support	Pore size (FWHM)	BET surface area	Pore volume (p/p_0)
Al_2O_3	8.7 nm (3.83)	172 m^2g^{-1}	0.46 cm^3g^{-1} (0.999)
MCM-41	2.7 nm (0.23)	1260 m^2g^{-1}	1.28 cm^3g^{-1} (0.994)
SBA-15	6.7 nm (1.27)	630 m^2g^{-1}	0.86 cm^3g^{-1} (0.993)
Al-SBA-15(20)	6.6 nm (1.22)	633 m^2g^{-1}	0.70 cm^3g^{-1} (0.998)
Al-SBA-15(10)	6.5 nm (1.12)	705 m^2g^{-1}	0.99 cm^3g^{-1} (0.999)
$NaBH_4@Al_2O_3$ 30%	8.6 nm	117 m^2g^{-1}	0.31 cm^3g^{-1} (0.997)

TABLE 3.1: Nitrogen physisorption analysis of supports used in this work and a 30% pore filling $NaBH_4@Al_2O_3$ composite.

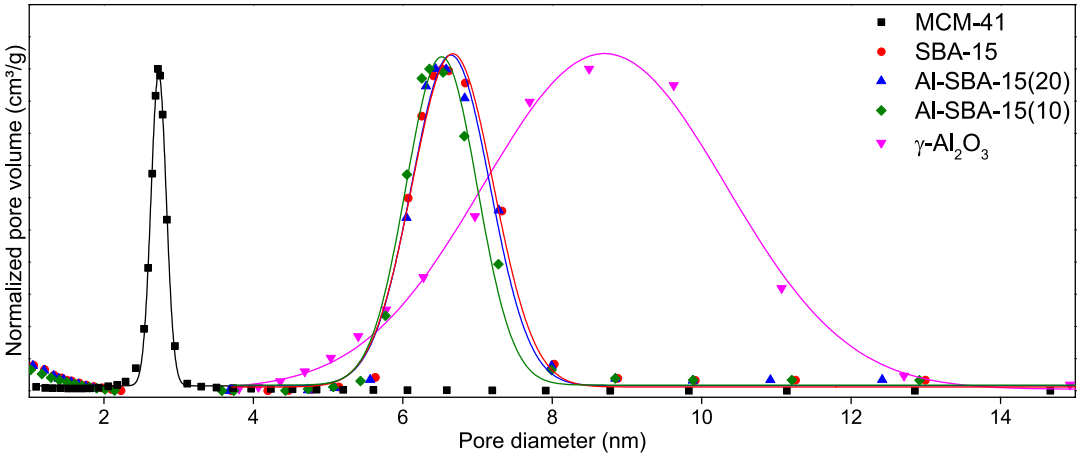

FIGURE 3.1: BJH pore size distributions of the supports used in this work.

To investigate the degree of infiltration of the electrolyte salts into the pores, $NaBH_4$-oxide composites were measured with nitrogen physisorption after melt infiltration. For both $NaBH_4@Al_2O_3$ and $NaBH_4$@MCM-41 the composites showed a lack of porosity (surface area <10 m^2g^{-1} and pore volume <0.066 cm^3g^{-1} normalized to the mass of the support). This loss of pore volume indicates either a complete pore filling or pore blocking of the entries of the pores. The latter explanation could cause inhibition of all pore entries and would not be desirable for the purpose of these melt infiltration, which was interface engineering of the salt in close proximity to the support.

To get a better idea of the pore filling mechanism, a 30% pore filling $NaBH_4@Al_2O_3$ composite was measured with nitrogen physisorption. The total pore volume per gram of support was determined as 0.36 cm^3g^{-1}. Note that this is slightly more than reported in Table 3.1, because of the small amount of $NaBH_4$ present in the composite. This pore volume after melt infiltration is in the range of the theoretical pore volume of a 30% filled support. This indicates that the pores of the Al_2O_3 are infiltrated, and thereby pore volume is lost, instead of blocking the entries of the pores.

To investigate the morphology of the Al_2O_3 and MCM-41 supports used in this work, SEM images were taken. In Figure 3.2 are depicted, single particles of Al_2O_3 and MCM-41 and further zoom on their surface. From Figure

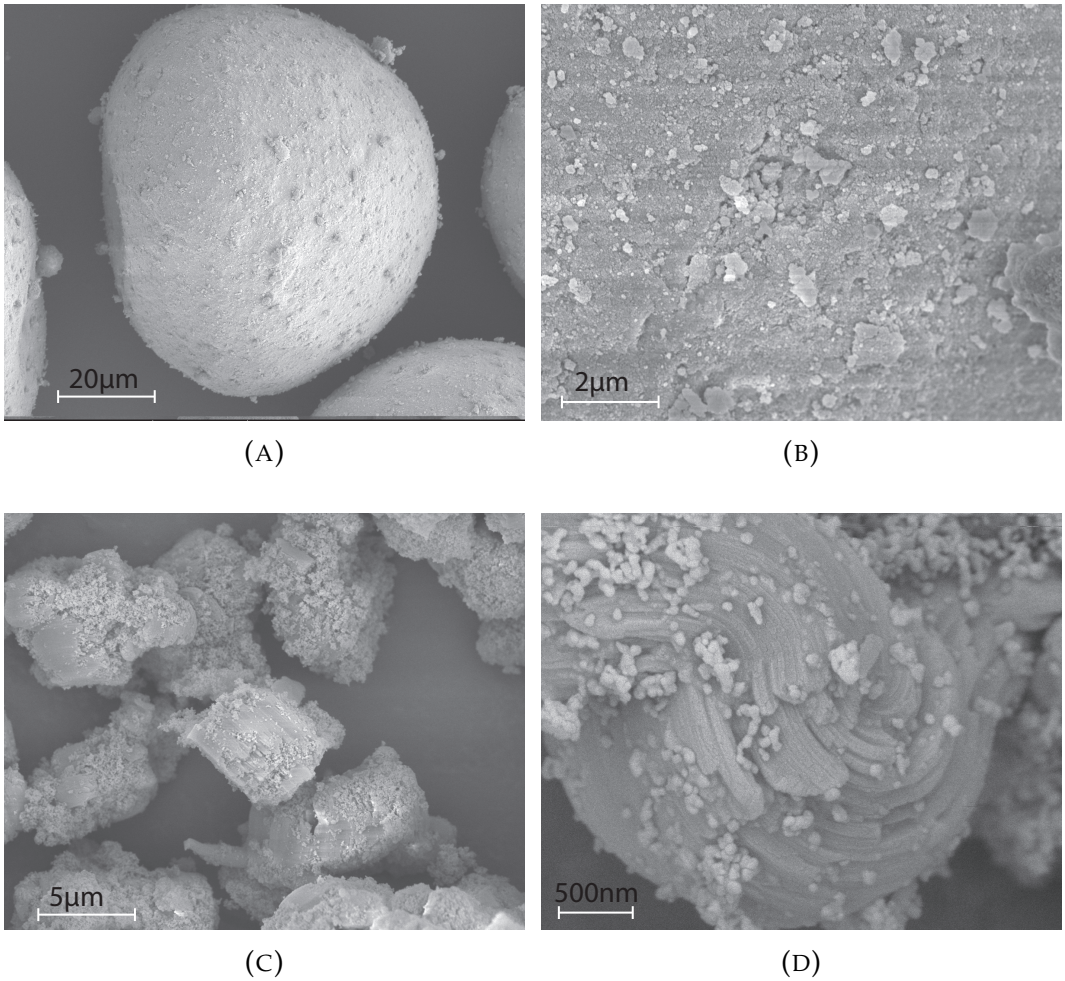

(A) (B)

(C) (D)

FIGURE 3.2: SEM images of (A,B) Al_2O_3 and (C,D) MCM-41.

3.2a it is seen that the commercial γ-Al_2O_3 consists of spherical-like particle grains 70-80 microns in diameter. A zoom in of the surface in Figure 3.2b shows the roughness of the support that explains the high surface area of these small particles. The disordered pores cannot be observed with the resolution of these images. In Figure 3.2c multiple grains of MCM-41 particles are observed with a typical particle width of 5-10 micron (note the difference in scale-bars between A and C). A zoom in of one MCM-41 grain in Figure 3.2d reveals the ordered one-dimensional channel pore structures. Some residual blobs of, what is believed to be, condensed silica is seen on top of the MCM-41 particle.

3.1.2 $NaBH_4$-oxide composites

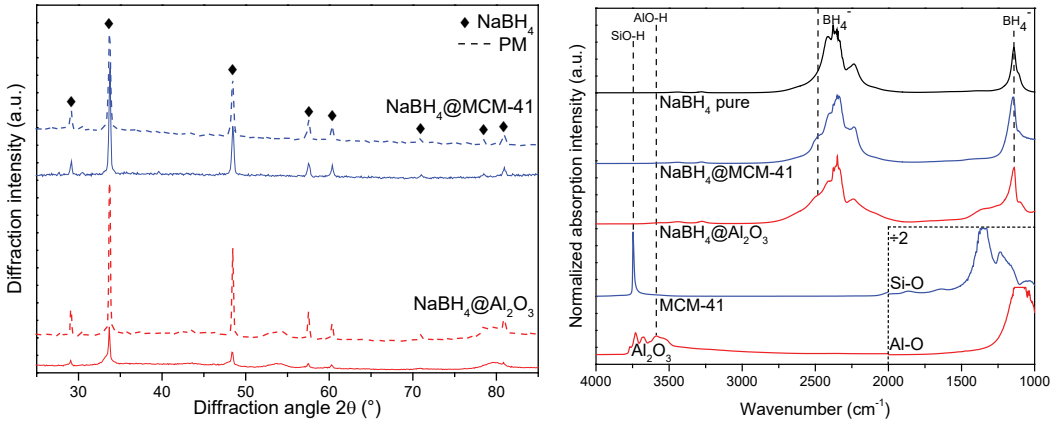

(A) (B)

FIGURE 3.3: (A) XRD patterns of $NaBH_4$@Al_2O_3 and $NaBH_4$@MCM-41 composites and their physical mixtures. (B) DRIFTS spectra of pure supports, $NaBH_4$, $NaBH_4$@Al_2O_3 and $NaBH_4$@MCM-41.

$NaBH_4$-oxide composites were prepared with melt infiltration as described in Section 2.2.2. The crystalline structure of the composites was investigated after synthesis with XRD. In Figure 3.3a the measured XRD patterns of $NaBH_4$ composites with 130% pore filling in Al_2O_3 and MCM-41 are shown in solid blue and red lines respectively. The dashed blue and red lines represent their physical mixtures (PMs, i.e. the starting materials) of the composites, that were used for the melt infiltration. The diffractograms were compared to a reference pattern of $NaBH_4$, indicated by the black diamond symbols.

From these patterns can be seen that during synthesis no new crystalline phases have emerged. This indicates the heating did not induce any decomposition into new crystalline compounds. Only diffraction peaks from $NaBH_4$ and the support were observed. From these patterns is concluded that after the melt infiltration the $NaBH_4$ has a face-centered cubic crystal structure with $F_{m\bar{3}m}$ symmetry which is in line with literature.[59,60]

Two broad diffraction peaks are observed for $NaBH_4$@Al_2O_3 around 54° and 80°, ascribed to Al_2O_3 as they are also observed for the physical mixture. MCM-41 shows no distinct diffraction peaks at these diffraction angles, as its repeating unit cell is at much larger pore-pore distances and thus much smaller diffraction angles $2\theta < 10°$. A small unknown impurity is found at 31°, which originates from the starting material of $NaBH_4$, as it is already present in the physical mixture, or could be from a strong diffraction peak of residual carbon contamination on the sample holder.

The $NaBH_4$@Al_2O_3 composite shows a decrease in diffraction intensity compared to the physical mixture. This could be caused by a lack of crystalline ordering of the $NaBH_4$ in contact with, or in the pores of, Al_2O_3. Another explanation of the decrease in diffraction intensity could be due to the formation of new non-crystalline material upon heating of $NaBH_4$. However,

this remains hard to ascribe by XRD, as no new diffraction pattern would be observed for such a non-crystalline material.

For $NaBH_4$@MCM-41 the diffraction intensity of the composite and physical mixture are almost identical and no lack of crystallinity is observed, although this would be expected when infiltrated in these smaller pores. Therefore it is suggested that the $NaBH_4$@MCM-41 composite is not infiltrated during the synthesis. With physisorption we observed no accessible pore volume for this composite, therefore a complete pore blockage is suggested. This is further substantiated by XRD measurements on $NaBH_4$@MCM-41 of different pore fillings. In Figure A.2a it is depicted that also at pore fillings below 100%, where with good infiltration only confined $NaBH_4$ would be present, a bulk-like crystalline pattern is observed.

To study the molecular vibrations in the composites before and after synthesis, DRIFTS analysis is performed on the composites and their starting materials. The spectra of $NaBH_4$, $NaBH_4$@MCM-41 and $NaBH_4$@Al_2O_3 composites after melt infiltration are depicted in Figure 3.3b. Their corresponding supports are shown in the less opaque lines. The intensities inside the box on the bottom right have been divided by a factor of two for visualization. To investigate the effect of the synthesis conditions, the $NaBH_4$ has been treated with the same synthesis conditions as the composites.

The oxide supports show surface hydroxyl peaks above 3500 cm^{-1} and framework-oxide bonds below 1500 cm^{-1}. From the MCM-41 spectra, it is concluded that this support was well dried, as no viscinally bound H_2O were found to be present besides the sharp isolated silanol peak at 3700 cm^{-1}.[61] For hydrated Al_2O_3 no clear peak changes are observed upon drying and the dryness of the support with similar drying steps is assumed.[62]

Comparing the composite spectra with their corresponding supports, the surface hydroxyl peaks have disappeared after melt infiltration. This is ascribed to a reaction between support and infiltrated salt where the labile -OH groups form an interaction with the $NaBH_4$. This is in line with the observation of interface engineering on $LiBH_4$-Al_2O_3 composites, where a B-O bond is found with near edge X-ray fine structure (NEXAFS) analysis.[37]

For $NaBH_4$ we expect vibrational peaks around 2396, 2282, 2216 and 1110 cm^{-1} ascribed to ν_3, ν_2+ν_4, $2\nu_2$ and ν_2 B-H stretches.[60,63] This peak pattern is visible in the pure spectra to the right of the dotted line at 2414, 2344, 2237 and 1141 cm^{-1}. The heat treatment induces no new peaks in DRIFTS and XRD (see Figure A.2b) and $NaBH_4$ is found not to react during this treatment.

A small contribution from two unknown peaks is observed above 3300 cm^{-1}. Similar vibrations are found in the literature for pristine $NaBH_4$.[64] The region of these peaks indicate a possible O-H stretching of adsorbed water, although no confirmation by H-O-H bending is found in the spectra.[60]

Previous ascribed peaks originating from the $NaBH_4$ are visible in the composite spectra. Additionally, a new peak appears for the composites at 2473 cm^{-1}, indicated by the dashed line. This peak at slightly higher wavenumbers is ascribed to B-H stretching in $Na_2B_{12}H_{12}$.[65] This indicates the presence of small amounts of $Na_2B_{12}H_{12}$ due to partial decomposition of $NaBH_4$. This formation is further supported by calculations of Liu et al.

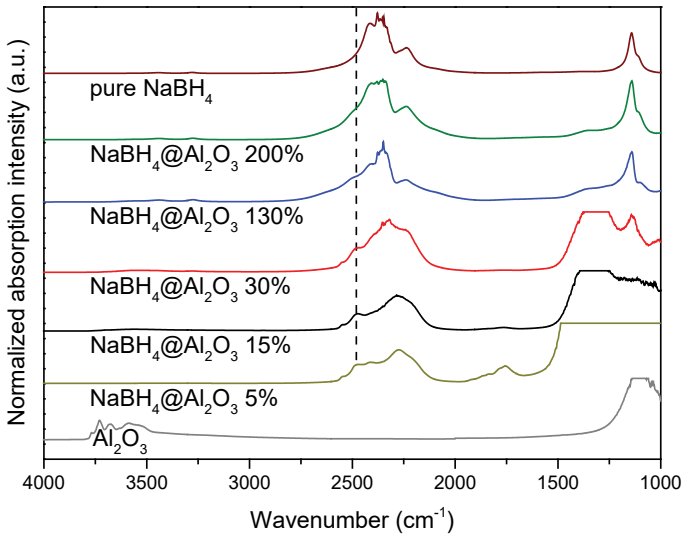

FIGURE 3.4: DRIFTS spectra of pure Al_2O_3, $NaBH_4$ and $NaBH_4@Al_2O_3$ composites with different pore fillings.

where is shown that $Na_2B_{12}H_{12}$ is a more stable species upon decomposition of $NaBH_4$.[66] This new contribution could be a (partial) explanation of the decreased diffraction intensity observed by XRD. Since the main diffraction peak of $Na_2B_{12}H_{12}$ is not found (see Figure A.3), it is ascribed to be amorphous.[65]

To further investigate the interfacial effect with DRIFTS, several low pore filling $NaBH_4@Al_2O_3$ composites were prepared. In Figure 3.4 the spectra of previous mentioned 130% and pure spectra are displayed together with a 200%, 30%, 15% and 5% sample. All spectra show no visible contributions from the alumina surface hydroxyl peaks, which further substantiates the hypotheses that the $NaBH_4$ has an interaction with the support, already at these low pore fillings, ascribed to well wetting of the alumina support by the melt infiltrated $NaBH_4$.

From these spectra, the contribution from the peak around 2473 cm^{-1} becomes more pronounced in the lower pore filling composites, while the bulk-like stretches become less pronounced. Below 30% pore filling a second contribution from the $Na_2B_{12}H_{12}$ B-H stretching at 2546 cm^{-1} is observed. This is in line with the two peaks observed for $Na_2B_{12}H_{12}$.[65] At higher pore filling, less pronounced signal is observed, hence it is believed that in the bulk-like environment this decomposition does not occur. Therefore, this formation of $Na_2B_{12}H_{12}$ is ascribed as an interfacial effect originating from the salt-oxide interface in the composite.

For the low pore filling composites, a contribution arises below 1500 cm^{-1}, at higher wavenumbers than the alumina framework Al-O bond. This large contribution matches the literature with borate-like B-O vibrations, which further confirms the hypotheses of B-O formation between the alumina -OH groups and the $[BH_4]^-$ anion.[67,68] This contribution overshadows the B-H stretches at 1110 cm^{-1} at 15% and 5% pore filling. At 5% pore filling an unknown peak at 1755 cm^{-1} emerged. This peak is not visible in the other composites and could be due to an unassigned surface effect or a small amount

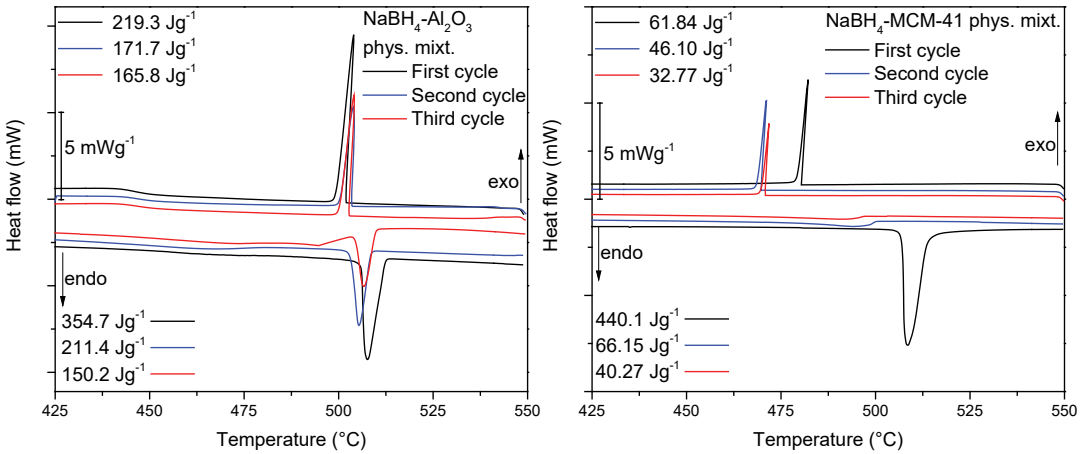

FIGURE 3.5: DSC curves of (A) $NaBH_4$-Al_2O_3 and (B) $NaBH_4$-MCM-41 physical mixtures cycled three times between 380 and 550°C with a 10°Cmin^{-1} heating and cooling ramp. Inset values represent the integral of the heat flow peaks in the curve.

of impurity, that was overshadowed in higher pore fillings.

Comparing the pure $NaBH_4$ absorption to the composites in Figure 3.3b and 3.4, a slight peak broadening is observed in all composite spectra. This is ascribed to a difference in crystallinity of the compound or symmetry of its structure compared to the bulk-like $NaBH_4$, which could occur from close proximity to, or in the pores of, the support.[69] This is in line with the observed loss in long-range crystallinity from XRD for $NaBH_4$@Al_2O_3, where the largest peak broadening is observed. The 130% pore filled $NaBH_4$@MCM-41, with a higher support surface area, shows less peak broadening than $NaBH_4$@Al_2O_3, which further substantiates the hypothesis from XRD, that the $NaBH_4$ is not well infiltrated in the pores of MCM-41.

To investigate the pore infiltration of $NaBH_4$ into the porous supports in the synthesis, DSC measurements under hydrogen pressure were performed with the $NaBH_4$-oxide physical mixtures. In this way, the first DSC cycle would simulate the melt infiltration step, whereas the later cycles represent the behaviour of melt infiltrated composites. Figure 3.5 depicts the thermogram for three consecutive cycles between 425 and 550°C.

From Figure 3.5a the melting of $NaBH_4$ in the first cycle has an onset of 505.9°C, peak at 507.7°C and integrated area under the curve (melting enthalpy) of 354.7 Jg^{-1} calculated to the mass of $NaBH_4$. This is below literature value of 447 Jg^{-1} for the melting enthalpy of $NaBH_4$, which indicates a partial reaction below the melting point of $NaBH_4$.[70] Upon solidification during cooling, the enthalpy decreases to 219.3 Jg^{-1}, which is a 38% decrease. This difference between melting and crystallization is attributed to further partial reaction upon melting or incorporation into the pores where the nanoconfined $NaBH_4$ shows less exothermic recrystallization.

In the second and third cycle, similar behaviour is observed. The melting point in the second cycle shows a slightly decreased onset and peak value

of 503.2°C and 505.4°C respectively. The melting and solidification enthalpy decrease from 211.4 Jg^{-1} to 171.7 Jg^{-1}. Note that the melting enthalpy in the second heating step has approximately the solidification enthalpy in the first cycle. This indicates that non-nanoconfined $NaBH_4$ melts in the next cycle. A further decrease in enthalpy upon cycling is ascribed to further infiltration of $NaBH_4$ material into the pores. The decomposition of the material is found not to be an explanation for this decrease in peak area, as no total mass loss is observed before and after the experiment. If decomposition occurred the release of hydrogen from the $NaBH_4$ would be noticed by a loss of mass. Due to an unexpected jump in the baseline in the third heating cycle, no quantitative analysis is performed on the melting and solidification enthalpy.

In Figure 3.5b the DSC curves from $NaBH_4$-MCM-41 are shown. In the first cycle, the melting enthalpy is (within rounding error) the same as for pure $NaBH_4$ (see Figure A.4) in line with reported literature values.[70] The composite melting peaks are slightly broadened compared to pure $NaBH_4$, due to the poor heat conductivity of the present oxide supports. Upon cooling the enthalpy decreases with 86% (from 440.1 to 61.84 Jg^{-1}) ascribed to a large amount of nanoconfinement. In the second and third cycle, the recrystallization enthalpy further decreases, due to more infiltration into the small pores. In this sample, a clear peak shift is observed between the first cycle and later cycles. This decrease in melting and crystallization temperature is due to nanoconfinement effects.[39] This is in contrast with observed results from XRD and DRIFTS, where was assumed that this composite was not well infiltrated during synthesis.

No mass loss is found after DSC, indicating no major decomposition combined with the release of molecular hydrogen. The large difference between $NaBH_4$@Al_2O_3 and $NaBH_4$@MCM-41 is ascribed to their difference in PSD: the Al_2O_3 has larger, less ordered pores and smaller pore volume, and therefore shows fewer confinement effects upon infiltration in the pores.

3.1.3 $NaNH_2$-oxide composites

$NaNH_2$-oxide composites were prepared as described in Section 2.2.2. The crystalline structure of the composites was investigated after synthesis with XRD. In Figure 3.6a the measured XRD patterns of $NaNH_2$ composites with 130% pore filling in Al_2O_3 and MCM-41 are shown in solid blue and red lines respectively. The dashed blue and red lines represent the physical mixtures of the composites.

From these patterns, it can be seen that the same crystalline phases from the physical mixtures are present after synthesis. Therefore it can be concluded that there is no decomposition of the material during the synthesis. Diffraction peaks from the $NaNH_2$ reference pattern, indicated by the black diamonds is observed in all spectra. Therefore, after melt infiltration, $NaNH_2$ has a face-centered orthorhombic crystal structure with F_{ddd} symmetry, which is in line with literature reports.[71,72] Similar to $NaBH_4$@Al_2O_3, a broad peak around 54° is observed, arising from the Al_2O_3 support. MCM-41

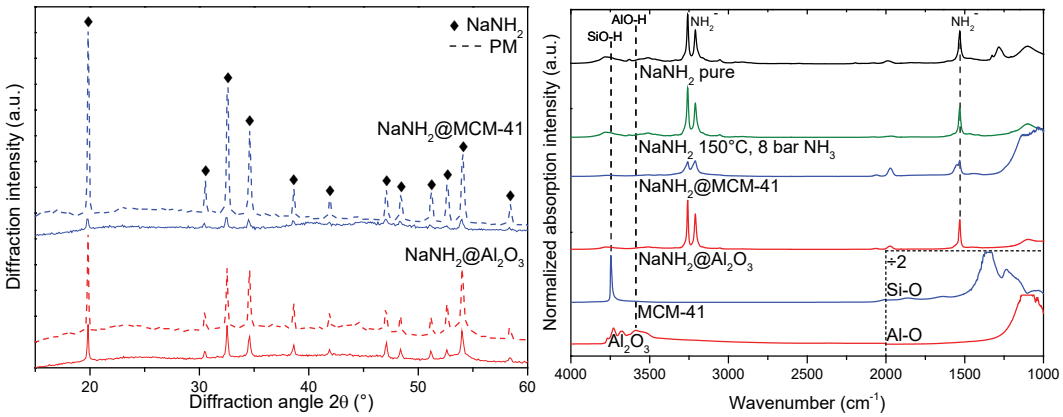

(A) (B)

FIGURE 3.6: (A) XRD patterns of $NaNH_2$@Al_2O_3 and $NaNH_2$@MCM-41 composites and their physical mixtures. (B) DRIFTS spectra of pure supports, $NaNH_2$, $NaBH_4$@Al_2O_3 and $NaBH_4$@MCM-41.

shows no distinct diffraction peaks at these diffraction angles, as its repeating unit cell is at much larger pore-pore distances and thus much smaller diffraction angles.

Although the measurement stepsize and time were the same for the physicals mixtures and their composites, a noticeable decrease in XRD peak intensity is observed. This could be due to incorporation in the pore of the support that inhibits long-order crystallization. This phenomenon is more pronounced in the $NaNH_2$@MCM-41 composite, which has smaller pores, higher surface area and higher pore volume. Formation of a non-crystalline phase is another explanation for this, yet is not possible to assign with certainty from this XRD measurement. It has been proposed than $NaNH_2$ in Argon atmosphere above 200°C decomposes to amorphous sodium amide imide releasing ammonia, described by $3\,NaNH_2 \longrightarrow Na_3(NH_2)(NH) + NH_3$.[51] This could explain the loss in diffraction intensity, indicating that the 8 bar of ammonia pressure used in the melt infiltration, was not sufficient for complete suppression of decomposition in this material.

To study the molecular vibrations in the composites before and after synthesis, DRIFTS analysis is performed on the composites and their starting materials. The DRIFTS spectra of $NaNH_2$, $NaNH_2$ heated under ammonia, $NaNH_2$@MCM-41 and $NaNH_2$@Al_2O_3 are depicted in Figure 3.6b. The treated $NaNH_2$ is measured to check if this pressure and elevated temperatures induce any spectral changes. The supports of these corresponding composites are shown in semi-transparent blue and red curves respectively. The support intensities in the box on the bottom-right have been manually divided by a factor of two for visualization purposes. Comparing the supports to their corresponding composites, the surface hydroxyl groups have disappeared after the synthesis. This is ascribed to a reaction between the infiltrated salt and the labile hydroxyl on the surface of the supports.

When comparing the untreated $NaNH_2$ to the same compound heated

for 2 hours at 150°C the disappearance of intensity around 1300 cm^{-1} is observed. Since this peak is not found in $NaNH_2$ literature, and from XRD no new phases are found, it is ascribed to the thermal removal of some of the impurities from the material. Note that this impurity has disappeared already at 150°C, which is below the used melt infiltration temperature of 225°C.

In the composites, the $NaNH_2$ peaks at 3260, 3210 and 1532 cm^{-1} are observed. These observed frequencies are ascribed to the ν_3, ν_1 and ν_2 vibrations respectively.[73] In particular, in $NaNH_2$@MCM-41 the peaks seem to show some broadening. This broadening could be ascribed to both mobile broadening or inhomogeneity close to the surface of the support. Small intensity around 2060 and 1970 cm^{-1} is observed for all $NaNH_2$ containing materials, although it seems more pronounced in the composites. No literature is found that report any signal within this spectral region.

In an effort to investigate the pore infiltration of $NaNH_2$ in the porous oxide supports, DSC measurements are performed on the $NaNH_2$-MCM-41 and $NaNH_2$-Al_2O_3 physical mixtures under 5 bar hydrogen pressures. Unfortunately, ammonia pressure was not possible to apply in the DSC set-up and therefore decomposition of the $NaNH_2$ could not be prevented. For both samples, significant mass loss was found afterward and no endothermic or exothermic heat flow was observed after decomposition in later cycles (see Figure A.5).

3.1.4 Non-hydride based composites

As shown before, melt infiltration has interesting results on the structural characterisation of light-weight metal hydrides. Therefore this approach is extended to the nanoconfinement of non-hydride based materials. Several non-hydride based sodium-salts have been prepared by melt infiltration as described in Section 2.2.2. This includes oxide based $NaNO_2$, $NaNO_3$ and $NaClO_3$ as well as $NaAlCl_4$.

Firstly the structural characterisation of $NaNO_2$ and $NaNO_3$ composites after synthesis is discussed by XRD and DRIFTS. The XRD patterns of the starting material salts together with their composites in Al_2O_3 and MCM-41 are depicted in Figure 3.7a for $NaNO_2$ on top and $NaNO_3$ on the bottom half of the Figure. From these patterns, it is concluded that these materials form no new phases upon melting as phase pure patterns in line with the reference patterns (displayed by the symbols) are obtained. A difference in relative intensities of the diffraction pattern is observed for the pure $NaNO_2$ and its composites. This indicates a difference in the preferential orientation of the crystals. The pattern of the composites gives the best match with reference patterns for $NaNO_2$ (PDF 00-006-0392 (ICDD, 2018)).

The molecular vibrations of $NaNO_2$ and $NaNO_3$ salts and corresponding composites are investigated by DRIFTS and spectra are depicted in Figure 3.7b. Note that these spectra are measured in regular absorption units, instead of K-M units, hence the broader peak contributions and background signal (see Section 2.3.3). From the absence of the surface hydroxyl peaks in the $NaNO_2$@MCM-41, in the upper blue curve, it is concluded that this melt

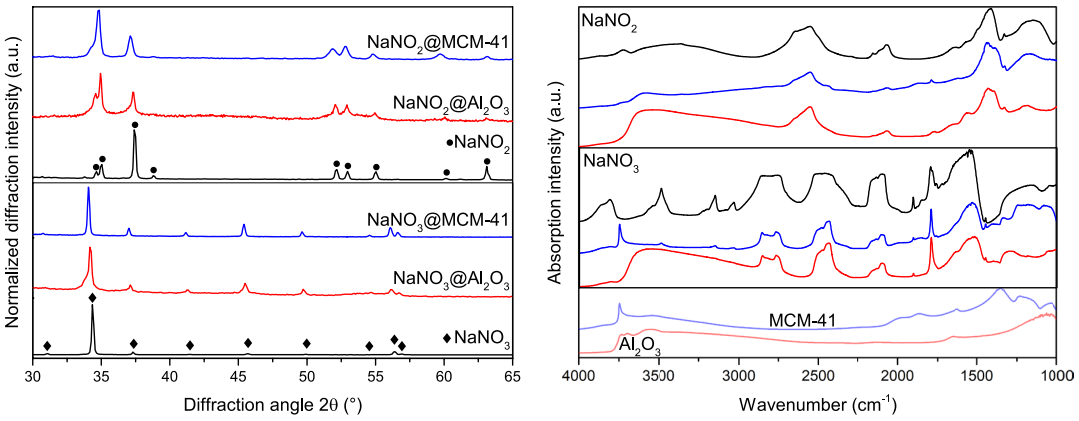

(A) (B)

FIGURE 3.7: (A) XRD patterns and (B) DRIFTS spectra of $NaNO_2$, $NaNO_3$ and their corresponding Al_2O_3 and MCM-41 composites.

infiltration was successful and a reaction with the support surface groups is observed. In $NaNO_2@Al_2O_3$ the broad surface signal from the Al_2O_3 support seems to remain present between 3700 and 3400 cm^{-1}, indicating a lack of infiltration in these pores, or no reaction with the surface hydroxyl groups. The spectral features of $NaNO_2$ were visible in both composites.

In the $NaNO_3$ composite spectra, the surface support hydroxyl surface peaks remain present after the synthesis for both supports. Therefore there is either no incorporation into the pores or no reaction with the hydroxyl peaks. The spectral features of $NaNO_3$ are clearly visible in the composite spectra, most prominent within the 3000 to 1500 cm^{-1} region.

For both $NaNO_2$ and $NaNO_3$ the interfacial effect of these composites do not look very promising. Combined with the fact that $NaNO_2$ has a poor ionic conductivity of itself, makes these composites not very promising for SSE applications.[74] The ionic conductivity measurements of these composites will be discussed in section 3.2.6.

The characterisation of $NaClO_3$ and $NaAlCl_4$ composites after synthesis is performed with XRD. The XRD patterns of $NaAlCl_4$ and $NaClO_3$ are shown together with their corresponding composites in Figure 3.8. In the pure salts, the patterns were an accurate match with reference patterns, indicated by the black diamond and circle symbols for $NaClO_3$ and $NaAlCl_4$ respectively.

From the XRD patterns of the composites, in all cases, decomposition into NaCl is observed. In the presence of the Al_2O_3 support, the salts decomposed completely into NaCl, as indicated by the reference pattern with the black club symbols and dashed lines. For the MCM-41 supported composites, a partial decomposition is observed, with the presence of the three NaCl peaks, as well as peaks from the starting materials sodium salt. Although decomposition of the pure salts was reported at higher temperatures, the presence of the support surface probably accelerated the decomposition to the thermodynamically more favorable NaCl.[44,75] The synthesis of these composites is therefore concluded not to be successful.

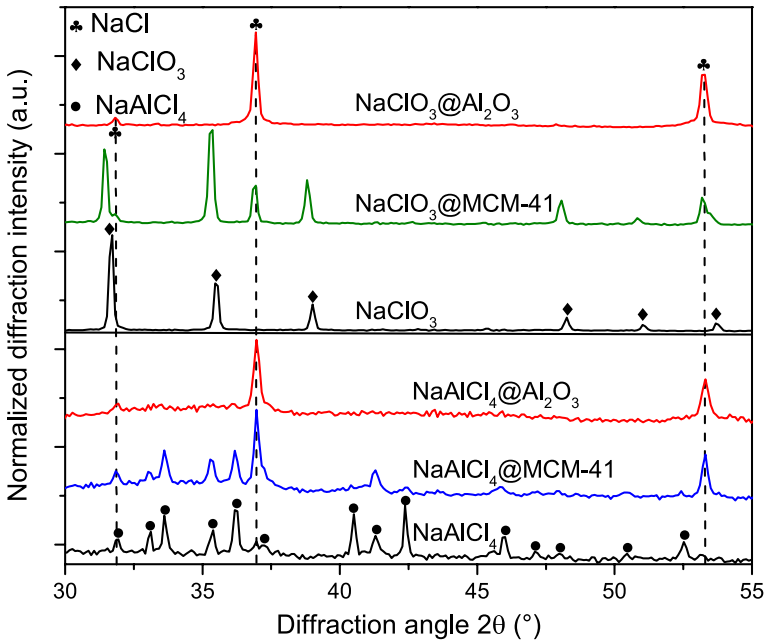

FIGURE 3.8: XRD patterns of $NaAlCl_4$ and $NaClO_3$ pristine material and composites.

3.2 Conductivity measurements

3.2.1 $NaBH_4$-oxide composites

Conductivity measurements of $NaBH_4$ and $NaBH_4$-oxide composites were performed with EIS, in a symmetrical cell using sodium electrodes. In Figure 3.9 the conductivity of untreated $NaBH_4$, $NaBH_4@Al_2O_3$ and $NaBH_4$@MCM-41 with a pore filling of 130% and are shown. Each symbol represents a single measurement at that temperature during heating (solid symbols) or cooling (open symbols). Shown data points are obtained from the second heating-cooling cycle between room temperature and 80°C.

The temperature dependence of the conductivity indicates Arrhenius type behaviour in the applied temperature range. This Arrhenius behaviour is described by

$$\sigma = Ae^{-E_{act}/k_B T}$$

where σ, E_{act}, k_B and T are conductivity, activation energy, Boltzmann constant and temperature respectively. The activation energy determines the slope of the temperature-dependent conductivity plots and is calculated from a linear fit of the logarithmic-reciprocal $\sigma - T$ plot. The standard error of the calculated value in its last digit is noted in the brackets in the figure. Note that this is the error of the temperature-dependent fit, and the inaccuracies in the obtained conductivity values itself are not taken into account.

By the observation of the reversible behaviour of the conductivity upon heating and cooling (the solid symbols overlay the open symbols), it is concluded that changes such as decomposition or phase change are negligibly small and the material is stable in the applied temperature window.

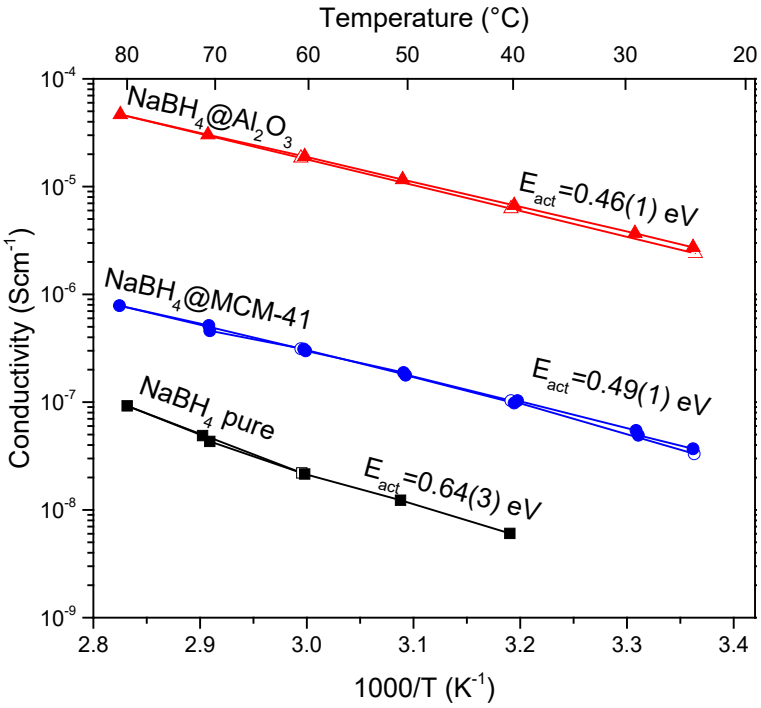

FIGURE 3.9: Temperature-dependent conductivity of $NaBH_4$, $NaBH_4@Al_2O_3$ and $NaBH_4$@MCM-41 obtained by EIS during heating (solid symbols) and cooling (open symbols). The activation energies are calculated from the slope of the plot.

In all cases the composites show higher conductivity than the pristine $NaBH_4$, despite less amount of $NaBH_4$ material is present per pellet thickness, due to the presence of the support. For comparison, the $NaBH_4$ mass fraction in Al_2O_3- and MCM-41-supported composites with a pore filling of 130% is 0.39 and 0.64 respectively. In addition to the enhanced conductivity, lower activation energy is obtained within this temperature range for both composites. The activation energies for the composites show comparable values, indicating a similar sodium hopping mechanism.

The $NaBH_4@Al_2O_3$ composite shows outstandingly higher conductivity compared to $NaBH_4$@MCM-41. This increase is ascribed to a strong interfacial effect that enhances the ionic conductivity of this particular salt-support combination. The relative conductivity of the composites compared to the pure $NaBH_4$ at 40°C is a factor 1000 for $NaBH_4@Al_2O_3$, while only a factor 20 for $NaBH_4$@MCM-41. This difference is particularly interesting since the MCM-41 support has much higher BET surface area, that may attribute to the interfacial effect (see Table 3.1). However, as seen from XRD and DRIFTS, this composites seems not to have infiltrated the pores. Therefore, interfacial effects would only be observed on the outside surface of the oxide particle, and not inside the pores. Further investigation of the interfacial effect in $NaBH_4@Al_2O_3$ will be described in Section 3.3.

The EIS measurements do not differentiate between electronic and ionic

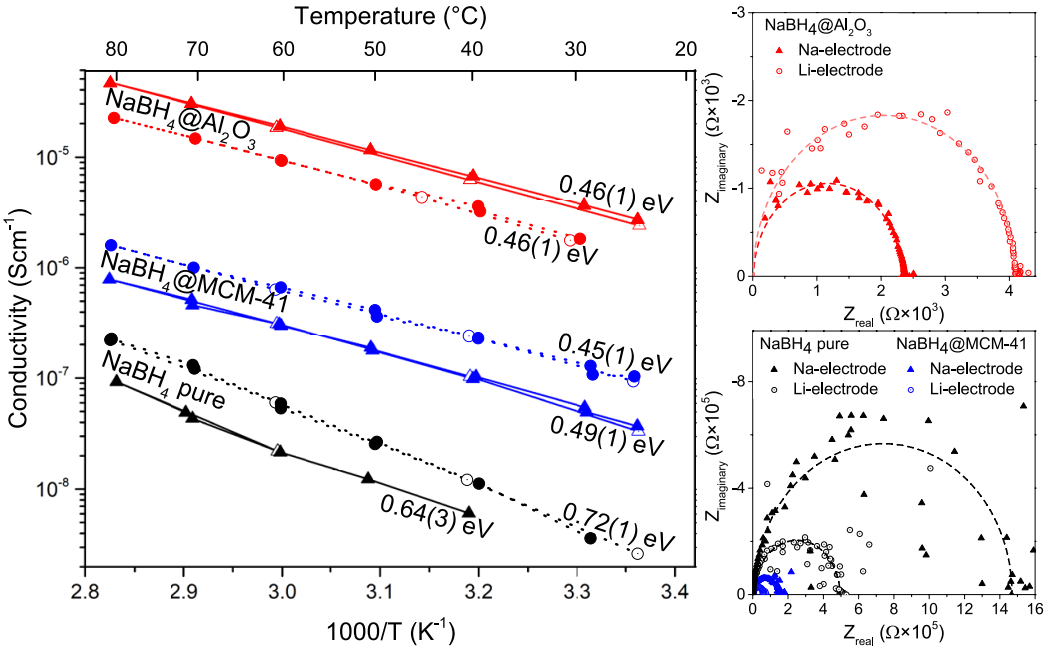

FIGURE 3.10: (A) Temperature-dependent conductivity of $NaBH_4$, $NaBH_4$@Al_2O_3 and $NaBH_4$@MCM-41 obtained by EIS during heating (solid symbols) and cooling (open symbols). The activation energies are calculated from the slope of the plot. (B) The complex impedance plots obtained at 80°C. Triangles and circles represent measurement performed with sodium and lithium electrodes respectively.

conductivity, and hence it is referred to in this work as conductivity. However, it is expected that the contribution of electronic conductivity is negligible due to the insulating nature of the γ-Al_2O_3, SiO_2 and $NaBH_4$, for which a band gap of over 6, 6.8 and 9.2 eV has been reported.[76–78]

3.2.2 Sodium *vs.* lithium electrodes

In this work, lithium foil has been used as a facile electrode material in the preparation of pellets for EIS measurements before sodium foil was available. Therefore, a comparison of sodium and lithium electrodes is made for $NaBH_4$ and $NaBH_4$-oxide composites. In Figure 3.10a the temperature-dependent conductivity of $NaBH_4$, $NaBH_4$@Al_2O_3 and $NaBH_4$@MCM-41 are shown, obtained with symmetric cells with sodium or lithium electrodes (triangles and circles respectively).

The difference in conductivity of the sample composite with different electrodes is always within a factor of two. This factor is assumed to be well in the same order of magnitude and could be attributed to an error in the pellet thickness assumed, as electrode thickness could be inconsistent. Moreover, the activation energies with both electrodes show similar values for the composites. Therefore it is concluded that the $NaBH_4$ does not react upon contact with the metallic lithium in these measurement conditions, and no

other conductive species is formed. A noticeable difference is observed between the electrodes when comparing the $NaBH_4$ plots in the black lines. This is explained by the fact that in the case of the lithium electrode pellet, the $NaBH_4$ had obtained the same heat treatment as the composites. This heat treatment, in theory, is a simple melting and recrystallization. A partial decomposition upon heating is excluded as an explanation, since $NaBH_4$ in absence of the oxide supports shows no decomposition, as confirmed by XRD and DRIFTS (see section 3.1.2).

However, better fitting of the complex impedance plots was possible for the heat treated $NaBH_4$ with lithium electrodes, over the untreated $NaBH_4$ with sodium electrodes. This could originate from a better contact with the electrode as the recrystallized $NaBH_4$ was thoroughly ground afterwards, while the untreated $NaBH_4$ may have been ground to a less extent. A worse contact could also come from the thinner prepared sodium electrodes, compared to the commercially available lithium electrodes.

In Figure 3.10b the complex impedance plots for $NaBH_4$, $NaBH_4@Al_2O_3$ and $NaBH_4$@MCM-41 at 80°C are shown for sodium and lithium electrodes, represented by solid triangles and open circles respectively. The semicircle behaviour is clearly seen in the composites. The intercept of the semicircles fit with the Z_{real}-axis confirm the factor two difference between the electrodes. The pure $NaBH_4$ shows a lot more noise in the complex impedance plot, making it more difficult to accurately fit a semicircle at lower temperatures. Still, the Z_{real}-intercept can be obtained for the lithium electrode around 0.5×10^6 and the sodium electrode at $1.5\times10^6\Omega$. indicated by the dotted line. The obtained sample resistance at each temperature is taken at the Z_{real} intersection on the right side of the semicircle (dotted line).

It is expected that lithium foil is a blocking electrode material for sodium-ion measurements. Therefore, blocking electrode behaviour such as electrode polarization, seen by a spike in $Z_{imaginary}$ in the low-frequency domain is expected. However, no spike is observed in the low-frequency domain of the complex impedance plots. Such electrode polarization was observed in this project the case of copper electrodes and has been reported for blocking electrodes such as molybdenum and gold in the literature.[25,26,30,31] The absence of this spike in the low-frequency domain might suggest intercalation of sodium ions in the lithium foil, upon the alternating current potential in the EIS measurement. A formation of $Na_{0.5}Li_{0.5}BH_4$ at the interface is suggested. This alloy was calculated to have an alloying energy of 0.02 eV.[79] Therefore, this alloy might form with the 20mV rms modulated alternating current potential applied in EIS measurements.

3.2.3 Influence of the pore filling

To investigate the pellet preparation technique and in search of an optimal pore filling, different pore filling samples of $NaBH_4@Al_2O_3$ composites were prepared and measured with EIS. In Figure 3.11a the calculated compressibility of the sample is plotted for different pore filling composites. This compressibility is described as the fraction of the measured pellet volume

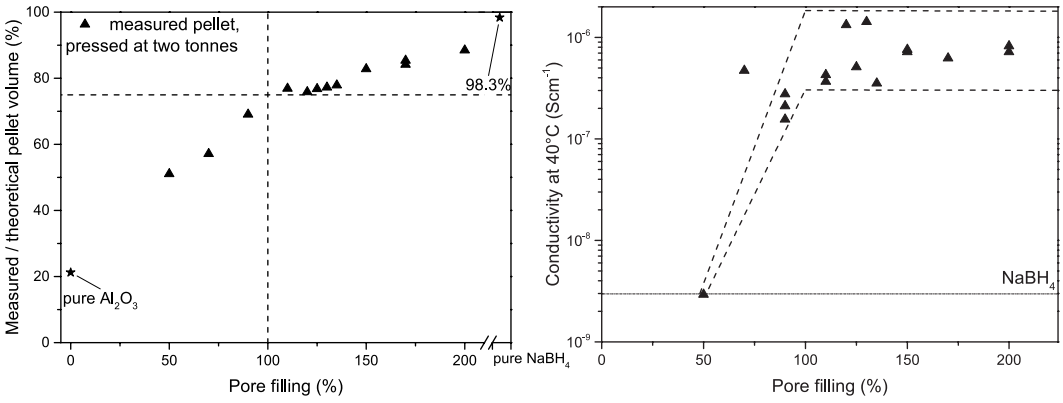

(A) (B)

FIGURE 3.11: (A) Compressibility and (B) conductivity at 40°C of different pore fill loading of $NaBH_4$@Al_2O_3 composites.

(with known pellet diameter and thickness, after subtraction of the lithium foil) compared to the theoretical volume. This calculation gives an indication of the void fraction in the pressed pellets. For the void fraction, the known starting material ratio is used in combination with assumed bulk densities of $NaBH_4$ and Al_2O_3 (1.074 and 3.980gcm^{-3} respectively). In all cases, lithium foil electrodes are used for their consistent thickness and prepared as described in Section 2.3.6.

The results in Figure 3.11a show a correlation of decreasing void fraction with increasing pore filling. When the starting material contained more than 100% pore filling, a filled fraction above 74%, which is the theoretical densest packing of perfect round spheres, was always found. When pressing pure Al_2O_3 or $NaBH_4$ a filled fraction of 21.3% and 98.3% is found respectively, which indicates a large amount of empty space in the porous alumina supports as well as the successful compressibility of the pure $NaBH_4$ with this pellet preparation.

These samples were also measured with EIS and their conductivity at 40°C is plotted in Figure 3.11b. The dotted horizontal line indicates the conductivity of the pure $NaBH_4$. From this figure, an increasing conductivity is observed from low pore filling to 100% pore filling. Above the 100% pore filling the conductivity is similar within the same order of magnitude. It is ascribed that above 100% the filling is sufficient for an optimal conductive pathway in the compressed pellet. The dashed lines are to guide the eye for the conductivity dependence on the pore filling. Note that the highest measured conductivity was at 130% pore filling and therefore this ratio is used in most composites preparations.

3.2.4 Aluminated SBA-15 composites

The large difference in the structure of the supports between $NaBH_4$@Al_2O_3 and $NaBH_4$@MCM-41 (Section 3.1.1) makes it difficult to compare the real

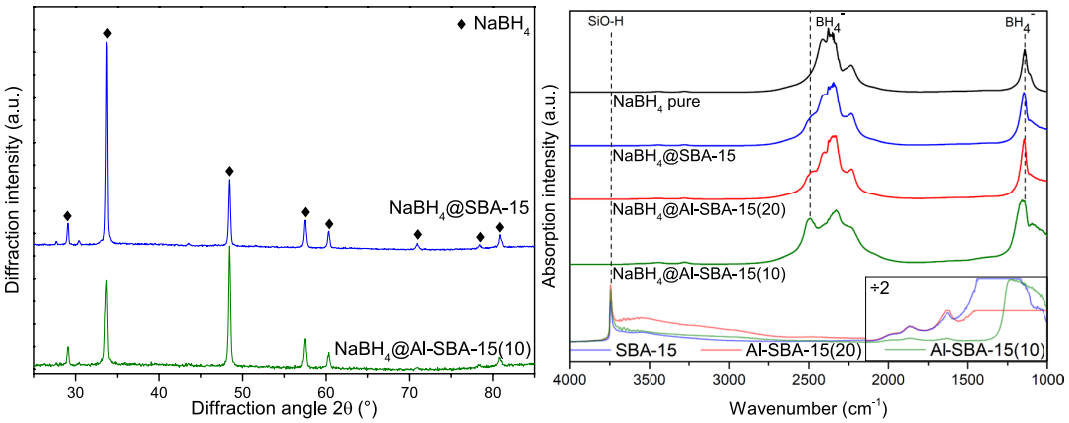

(A) (B)

FIGURE 3.12: (A) XRD patterns and (B) of (aluminated) SBA-15 composites and their starting materials.

impact on the measured conductivity (Section 3.2.1). To get a better comparison of the interfacial effect between silica and alumina, a model system of (aluminated) SBA-15 samples was used. Three supports with similar PSDs, but different Si/Al ratios were used for the melt infiltration of $NaBH_4$. The hypotheses of previously described conductivity results would suggest a stronger enhancement for SBA-15 with more alumina i.e. a lower Si/Al ratio. Two samples with Si/Al ratios of 20 and 10 were prepared, consequently named Al-SBA-15(20) and Al-SBA-15(10). The alumina amount is still relatively low, with the advantage that it has little to no effect on the PSDs and the support can be used in a comparative manner.

After melt infiltration of $NaBH_4$ into these supports, a brown powder was obtained for the $NaBH_4$@Al-SBA-15(20) and $NaBH_4$@SBA-15 composites, while both starting materials were white, indicating a reaction of these samples during synthesis. The $NaBH_4$@Al-SBA-15(10) composite, where exact same synthesis procedure was applied, did show to be a white powder after synthesis. After remeasuring the (aluminated) support with nitrogen physisorption, it was found that the support pore volume was overestimated, and an incorrect pore volume was used in these composites. This resulted in a large excess of pore filling, where for the brown powders over 250% of the pore volume was added. The $NaBH_4$@Al-SBA-15(10) composite had a less severe overestimation of the pore volume, which resulted in approximately 150% pore filling. Although the powders underwent a clear colour change, ascribed to an unwanted reaction, from XRD no new phases are found (see Figure 3.12a).

In Figure 3.12b the DRIFTS spectra of $NaBH_4$ is shown together with the (aluminated) SBA-15 composites and their corresponding supports. In all composite spectra, the surface isolated silanol peak shows no intensity around 3700 cm^{-1} after synthesis. This is ascribed to the interaction of the support with the $NaBH_4$. The vibrations of pure $NaBH_4$ between 2400 cm^{-1} and 2200 cm^{-1} as well as at 1100 cm^{-1} are visible in all composites.

A peak arises around 2500 cm^{-1} for the composites, as was similarly

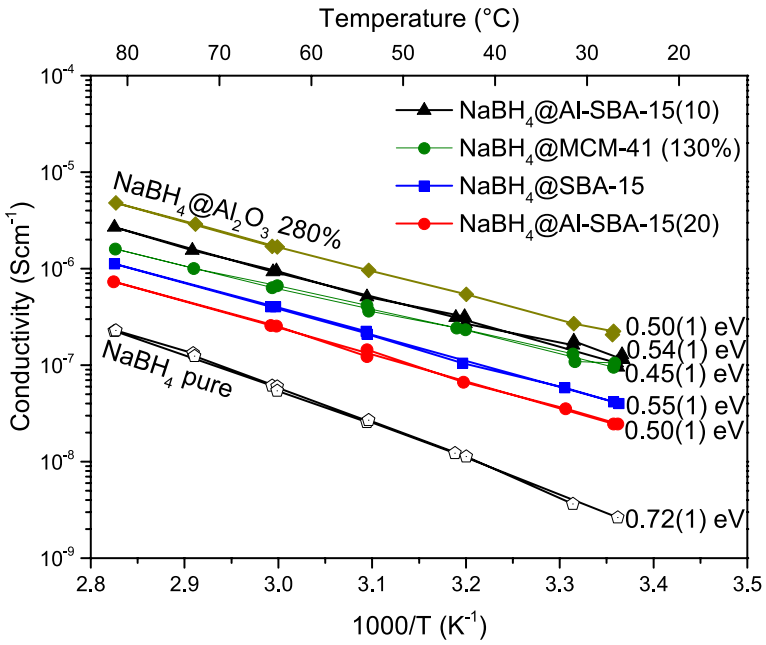

FIGURE 3.13: Temperature-dependent conductivity of $NaBH_4$ and $NaBH_4$-composites with MCM-41, (aluminated-)SBA-15 and Al_2O_3 supports obtained by EIS upon heating and cooling. Activation energies are calculated from the slope of the plot.

observed for the $NaBH_4@Al_2O_3$ and $NaBH_4$@MCM-41 composites (Section 3.1.2). This peak is most prominent for the $NaBH_4$@Al-SBA-15(10) composite, with higher intensity than was observed for $NaBH_4@Al_2O_3$. This peak is ascribed to stretching B-H vibrations in $Na_2B_{12}H_{12}$. This is further demonstrated by the broader peak around 1100 cm^{-1}, which is also found in the $[B_{12}H_{12}]^{2-}$ anion vibrations.[80]

The peak of the borohydride vibrations shows the largest broadening for $NaBH_4$@Al-SBA-15(10). This indicates the largest difference in crystallinity of the compound or symmetry of its structure compared to bulk-like $NaBH_4$, in presence of the Al-SBA-15(10) support.[69]

The results of this synthesis were not as desired, but the samples are still measured in a symmetrical cell with lithium electrodes for their conductivity and compared with the Al_2O_3 and MCM-41 supports. In Figure 3.13 the temperature-dependent conductivity of the (aluminated) SBA-15 are shown together with pure $NaBH_4$, $NaBH_4$@MCM-41 and $NaBH_4@Al_2O_3$ composites with 130% and 280% pore filling respectively. These composites are added to the plot for comparison of similar pore filling samples with the aluminated SBA-15 samples. The activation energy is depicted at the room temperature measurement symbol for every sample.

From the figure, it is seen that all the composites show enhanced conductivity and lower activation energy compared to the pure $NaBH_4$. When comparing the composites with a high excess of pore filling (>250%, blue and red curves), the SBA-15 (without alumina) shows higher conductivity than Al-SBA-15(20). This is at odds with the hypotheses, although the aluminated SBA-15 does show lower activation energy and may be within the

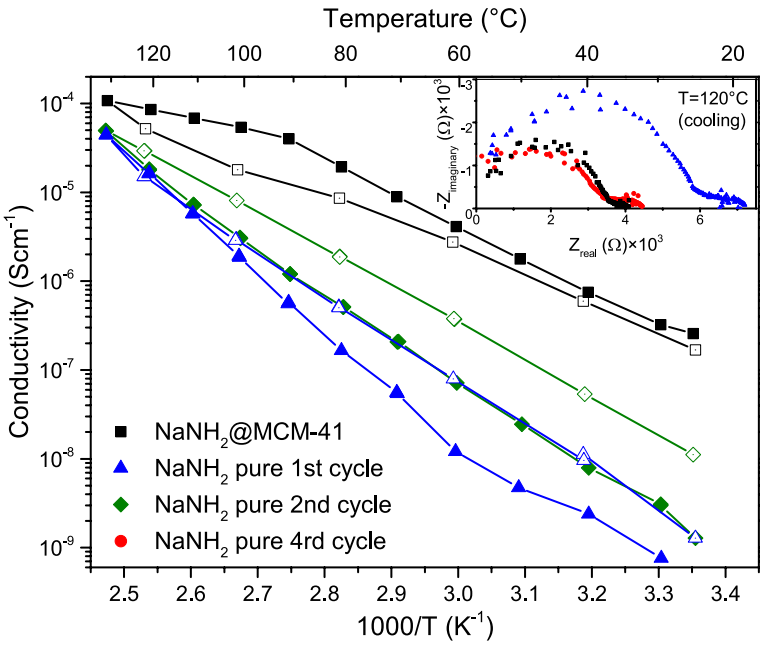

FIGURE 3.14: Temperature-dependent conductivity of $NaNH_2$@MCM-41 and $NaNH_2$ obtained by EIS during heating (solid symbols) and cooling (open symbols). The inset shows the complex impedance plots of $NaNH_2$@MCM-41 and $NaNH_2$.

error of the measurement. Both of these composites, however, show an order of magnitude lower conductivity than the 280% pore filling $NaBH_4$@Al_2O_3 composite.

Al-SBA-15(10) shows the highest conductivity of the (aluminated) SBA-15 samples, ascribed to the highest alumina loading. Although the amount of alumina is still quite low compared to the silica, it shows enhanced conductivity in the room temperature to 80°C temperature region compared to the 130% $NaBH_4$@MCM-41 composite. The activation energy of the MCM-41 support composite is still the lowest observed. This result remains difficult to compare as the pore sizes and surface areas are quite different.

3.2.5 $NaNH_2$-oxide composites

Besides the borohydride systems, the lightweight metal hydride $NaNH_2$ is investigated as a potential SSE candidate. In the literature, studies on the conductivity of $NaNH_2$ itself are somewhat overshadowed, as most research shows interest in the complex mixture of $Na_2(BH_4)(NH_2)$.[30] A possible reason for the lack of attention towards $NaNH_2$ could be the high activation energy and low conductivity at ambient temperatures, for example, an order of magnitude below $NaBH_4$. Here, the interface engineering approach is applied to $NaNH_2$ to obtain enhanced room temperature conductivity.
In Figure 3.14 the temperature-dependent conductivity of 130% pore filling $NaNH_2$@MCM-41 is shown in the black curve, measured in a symmetrical cell with lithium foil electrodes. From the non-reversible behaviour within

the cycle regarding conductivity and temperature dependent slope, it is concluded that the sample has a change in composition or phase when heated.

To investigate any change of the material a pellet of pure $NaNH_2$ pressed between lithium foil electrodes was prepared and cycled between room temperature and 130°C four times. Upon cycling, the conductivity increased each cycle. The complex impedance plots at 120°C (the first cooling step) of the first and fourth cycle shows this increase in conductivity by the decrease in resistance.

After the measurement, small bubbles of a metallic colour were observed on the pellet (see Figure A.6a). When analyzing the composition with DSC, it was confirmed to be metallic sodium (see Figure A.6b). The melting of this sodium explains the change of slope in the Arrhenius plot for $NaNH_2$@MCM-41 above 90°C ($T_m = 98.8$°C), as it changes the electronic conductivity. The formation of metallic sodium is suggested to be because of a reaction between the lithium foil and the $NaNH_2$ salt upon cycling, as follows: $NaNH_2 + Li^0 \longrightarrow LiNH_2 + Na^0$.

Thermodynamics confirm the possibility of this reaction, as the standard Gibbs free energy of formation for $LiNH_2$ (ΔG_f^0 = -140.6 kJmol^{-1}) is lower and thus more stable species than $NaNH_2$ (ΔG_f^0 = -64.0 kJmol^{-1}).[81,82] Therefore after such decomposition of $NaNH_2$, the $LiNH_2$ species is actually measured by EIS. Note in all cases a second semicircle is present in the low-frequency domain, indicating the presence of at least two conducting materials in the pellet. This could be ascribed to $LiNH_2$ with unreacted $NaNH_2$, still present in the sample. Another explanation of this second compound and overall high conductivity is the formation of Li_2NH (ΔG_f^0 = -169.9 kJmol^{-1}).[81] However, this highly conductive compound is reported to be synthesized at a much higher temperature than applied here.[83]

From this observation, $NaNH_2$ is concluded not to be compatible with lithium foil electrodes. The lithium foil showed no problems in the case of EIS measurements with $NaBH_4$ (see Section 3.2.2). The standard Gibbs free energy of formation $NaBH_4$ is comparable to $LiBH_4$ ((ΔG_f^0 = -123.7 kJmol^{-1} versus -125.0 kJmol^{-1}). $LiBH_4$ is slightly more stable (at 298K) but its lower entropy versus $NaBH_4$ (75.8 versus 101.2 JK^{-1}mol^{-1} respectively) makes $NaBH_4$ the more stable compound slightly above room temperature (see Figure A.7).[82]

Because of the instability of $NaNH_2$ in contact with lithium, conductivity measurements with sodium electrodes were required for the $NaNH_2$ samples. Temperature-dependent conductivity of $NaNH_2$, $NaNH_2$ heated under ammonia, $NaNH_2$@Al_2O_3 and $NaNH_2$@MCM-41 are shown in Figure 3.15. The treated $NaNH_2$ was measured as a reference to check if melting under ammonia pressure caused any deviation in the conductive behaviour of the salt. The data of the pure $NaNH_2$ illustrates its high activation energy and low conductivity, causing the problem that below 60°C no semicircle could be fitted through the data in the complex impedance plots.

A large enhancement of conductivity and decrease of activation energy is observed for the heat treated $NaNH_2$, and similarly for $NaNH_2$@Al_2O_3.

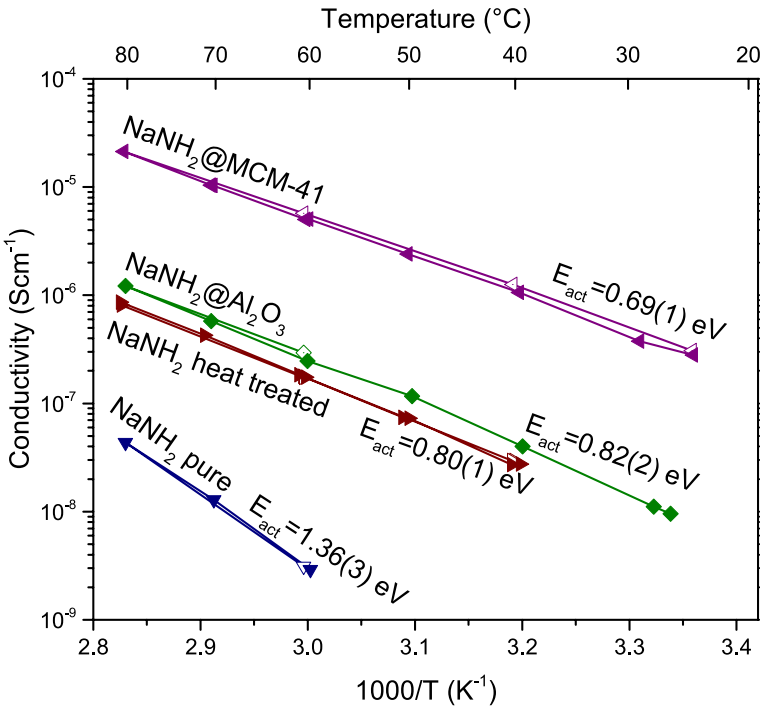

FIGURE 3.15: Temperature-dependent conductivity of $NaNH_2$@MCM-41, $NaNH_2$@Al_2O_3 and $NaNH_2$ as-received or with heat treatment obtained by EIS during heating (solid symbols) and cooling (open symbols). The activation energies are calculated from the slope of the plot.

As the enhancement already arises from the synthesis conditions, the interfacial effect is determined to be rather small or negligible for this composite. The enhancement could be due to insufficient ammonia pressure during the synthesis. A suggested decomposition product of $NaNH_2$ is $Na_3(NH_2)(NH)$, which is assumed to be an amorphous solid as literature and this work shows no XRD peaks from such a phase.[51] This could be a possible explanation for the enhanced conductivity as similar findings are reported for the decomposition of $LiNH_2$ to Li_2NH.[83]

The $NaNH_2$@MCM-41 composite shows the highest conductivity and lowest activation energy. There is a remarkably inverse behaviour compared to interface engineering on $NaBH_4$ where the Al_2O_3 support showed the most enhancement. This could be explained by the lack of crystallinity in the $NaNH_2$@MCM-41 composite that was found with XRD. This non-crystalline material could be described by a disordered $NaNH_2$ phase or $Na_3(NH_2)(NH)$ phase as such as described before. In either case it is shown that the presence of the MCM-41 support strongly improves the properties of this material as a candidate for SSE. Similar to $NaBH_4$, it is expected that the contribution of electronic conductivity is negligible due to the insulating nature of the oxide support and $NaNH_2$, for which a band gap of over 3.5 eV has been reported.[84]

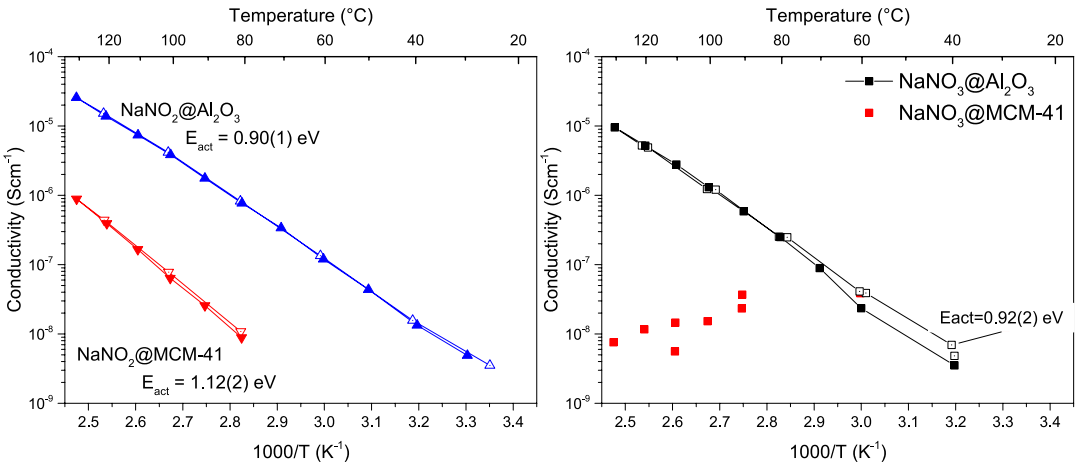

FIGURE 3.16: Temperature-dependent conductivity of (A) $NaNO_2$ and (B) $NaNO_3$ composites in Al_2O_3 or MCM-41 during heating (solid symbols) and cooling (open symbols). Activation energies are calculated from the slope of the curve.

3.2.6 Non-hydride based composites

From previous results, it is found that hydride based materials such as $NaBH_4$ and $NaNH_2$ show interesting results when melt infiltrated in oxide support. To investigate the effect of the interaction with the support on the conductivity the anion was varied to non-hydride based sodium salts. In this work $NaNO_2$, $NaNO_3$, $NaClO_3$ and $NaAlCl_4$ composites were prepared as described in Section 3.1.4. It was found that during the synthesis $NaClO_3$ and $NaAlCl_4$ decompose into NaCl, which has very poor ionic conductivity and will therefore not be measured on their conductive properties.

The temperature-dependent conductivity of $NaNO_2$- and $NaNO_3$-oxide composites are shown in Figure 3.16. The reversible behaviour upon heating and cooling suggests the samples are stable in this temperature range. $NaNO_3$ showed no detectable conductivity, as in the complex impedance only instrumental noise was observed. This is attributed to poor interfacial contact of this non-infiltrated composite, in line with the structural characterisation in in 3.1.4. The measured conductivity of these materials is low compared to hydride based materials and the high activation energy confirms the pessimistic hypothesis that was obtained from the structural characterisation. Although for $NaNO_2$-oxide composites different enhancement is found between the supports, no applications at ambient temperatures can be realized with these compounds.

3.2.7 Summary

In this section, the results of the EIS measurements on SSE candidates are discussed. $NaBH_4$-oxide composites were measured successfully with both sodium and lithium foil electrodes. It is proposed that in the latter an alloy of for example $Na_{0.5}Li_{0.5}BH_4$ is formed. Both electrode materials show similar conductivity and activation energy values, which were always better performing for the composites compared to the pure $NaBH_4$. $NaBH_4@Al_2O_3$ is investigated on an optimum pore filling fraction. This was found the be 130%, with the highest obtained room temperature conductivity in combination with the lowest activation energy 2.7×10^{-6} Scm^{-1} and 0.46 eV respectively. $NaBH_4$@MCM-41 shows similar activation energies but generally 1-2 orders of magnitude lower conductivity.

$NaNH_2$ was found unstable upon contact with lithium foil electrodes, indicated by a formation of $LiNH_2$ and metallic sodium. With a symmetrical cell with sodium foil electrodes, an enhancement in the composites is found by higher conductivity and lower activation energy compared to untreated $NaNH_2$. $NaNH_2$@MCM-41 with 130% pore filling measurements showed a room temperature conductivity of 3.1×10^{-7} Scm^{-1} with an activation energy of 0.69 eV. $NaNH_2@Al_2O_3$ showed almost identical conductive behaviour as heat treated $NaNH_2$ thus no interfacial effect is observed.

$NaNO_2$- and $NaNO_3$-oxide composites showed a low conductivity and high activation energy in the range of $\sim10^{-10}$ Scm^{-1} and $\sim$1 eV.

Both $NaBH_4@Al_2O_3$ and $NaNH_2$@MCM-41 with 130% pore filling exceed the previously reported metal hydride SSEs Na_3AlH_6.[31] $NaBH_4@Al_2O_3$ even exceeds the promising $Na_2BH_4NH_2$ SSE candidate.[30] An overview of the relevant results obtained with EIS in this thesis is provided in Table A.3.

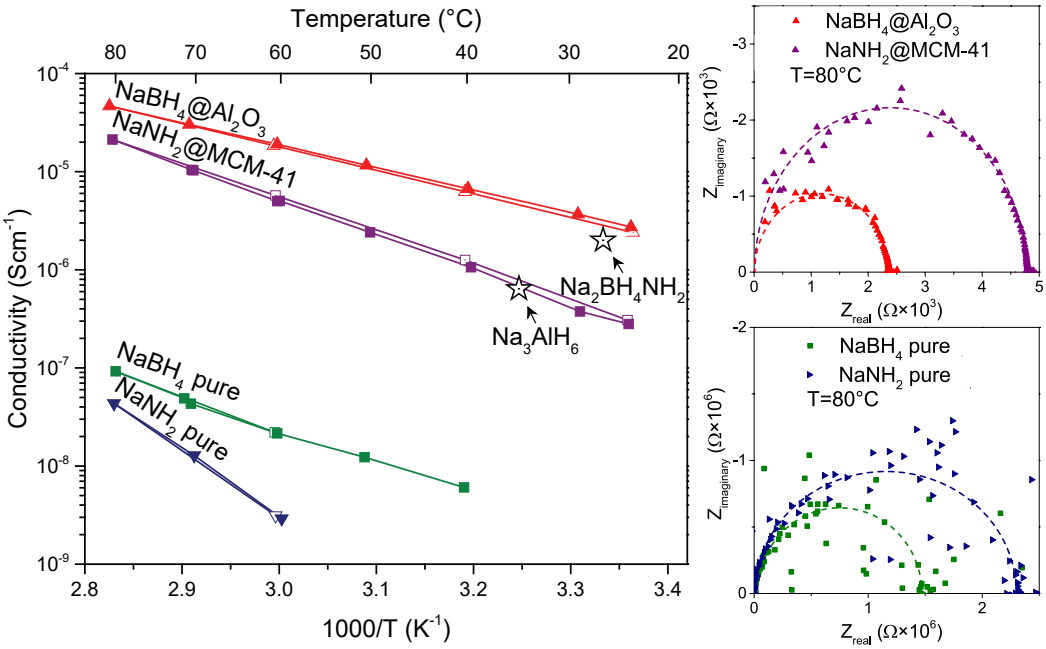

(A) (B)

FIGURE 3.17: (A) Temperature dependent conductivity of $NaBH_4$, $NaBH_4@Al_2O_3$, $NaNH_2$ and $NaNH_2$@MCM-41 obtained with EIS in the second heating (solid symbols) and cooling (open symbols) cycle. The values of the activation energies were calculated from the fit of an Arrhenius plot. $Na_2BH_4NH_2$ and Na_3AlH_6 are added for a comparison of metal hydrides, reproduced from Ref.[30] and Ref.[31] (B) The complex impedance plots of EIS measurements obtained at 80°C.

3.3 Nature of the $NaBH_4$-Al_2O_3 interface

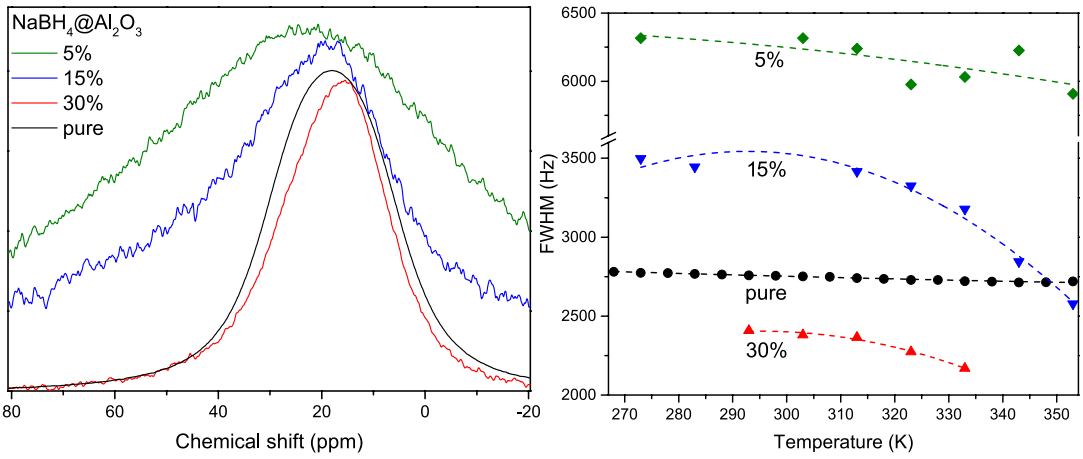

(A) (B)

FIGURE 3.18: (A) Static ^{23}Na NMR spectra obtained for pure $NaBH_4$ and low pore filling $NaBH_4@Al_2O_3$ composites at 313K. (B) Temperature dependence on the ^{23}Na peak width (FWHM).

To investigate the origin of the conductivity enhancement in $NaBH_4@Al_2O_3$ composites, solid-state NMR measurements were performed. For investigation of the $NaBH_4$-Al_2O_3 interface, samples with low pore filling are prepared, as in high pore fillings bulk-like peaks would dominate the spectrum. As reported in the literature on NMR measurements with nanoconfined $LiBH_4$@MCM-41, a narrow and a broad component are found in the ^7Li and ^{11}B spectra.[34,85] There, the narrow component is ascribed to a highly mobile species. The static ^{23}Na in $NaBH_4@Al_2O_3$ composites were measured to see if such a narrow peak in the composites is found.

Figure 3.18a shows the static ^{23}Na spectra averaged over 3456, 2048, and 16000 scans for pure $NaBH_4$, 30%, and 5%/15% $NaBH_4@Al_2O_3$ respectively, obtained at 313K. The spectra are normalized to the maximum intensity. The hypothesis of enhanced conductivity with interface engineering is attributed to highly mobile ionic species in close proximity to the oxide support.[86] However, the lowest pore fillings show broader peak widths, differing from the ^7Li hypotheses of narrow features for mobile ions.[34,85]

The temperature dependence of the peak width is investigated between 273 and 353K. In Figure 3.18b the peak widths obtained at different temperatures are plotted (the dashed lines are a trend to guide the eye). The pure $NaBH_4$ shows no change within this temperature regime, indicating its mobility range is outside of the line shape analysis range of this measurement. For the composites, temperature dependence is found resulting in more narrow peaks upon higher temperatures, in line with results from ^7Li NMR.[34,85] This narrowing could indicate higher mobility although a change in quadrupole coupling constant or combination of both effects cannot be excluded from these measurements.

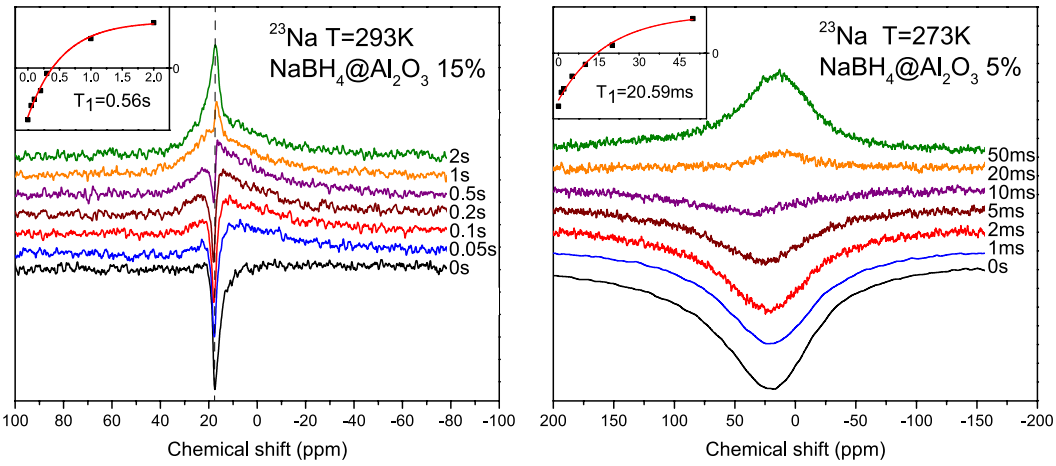

(A) (B)

FIGURE 3.19: Inverse recovery method for ^{23}Na in (A) $NaBH_4@Al_2O_3$ 15% and (B) $NaBH_4@Al_2O_3$ 5% obtained at 293K with 12kHz MAS and 273K without spinning respectively. Insets display the exponential fit to the obtained peak heights at different waiting times.

Upon further inspection of the 15% composite it was found that it consisted of a broad and a narrow component, similar to $LiBH_4$@MCM-41.[34,85] These peaks where not resolvable in the static measurements (Figure 3.18). To differentiate between these two peaks, relaxation time measurements are performed on 15% and 5% composites using the inversion recovery method.[87] In this method the nuclei spins are inverted by a 180° pulse, followed by a variable waiting period, after which a 90° pulse measures a regular NMR spectrum. The variation in waiting time ,t, will result in a fully inverted spectrum at $t = 0$, zero intensity at $t = T_1 \times ln(2)$ and a regular spectrum at $t >> T_1$, where T_1 is the spin-lattice relaxation time of the nuclei.

The spectra obtained with the inverse recovery method for the 15% composite are shown in Figure 3.19a, where at $t = 0s$ a complete inversion is observed for both the narrow and broad feature. Already at $t = 0.05s$ the positive intensity of the broad feature is visible in the spectra, while the sharp feature remains near completely inverted. A positive intensity is observed for the sharp feature after longer waiting times. This indicates the faster spin-lattice relaxation time of the broad component, compared to the narrow feature in this sample. The peak height of the sharp feature (along the dotted line) at different waiting times is plotted in the inset on the top-left of the figure. The red line in the inset shows the exponential fit of the measured data points (black symbols) at different waiting times. From this fit in the form of $y = y_0 + A \exp(-t/T_1)$ the spin-lattice relaxation time, T_1 is calculated. For the sharp feature, this was found to be 0.56 seconds. In the intensities of the sharp feature, there is interference of the positive broad contribution, and the precise T_1 should be slightly higher.

In the spectra of the 5% composite, no sharp feature is present and only the broad feature, ascribed to be in close proximity to the alumina interface, is

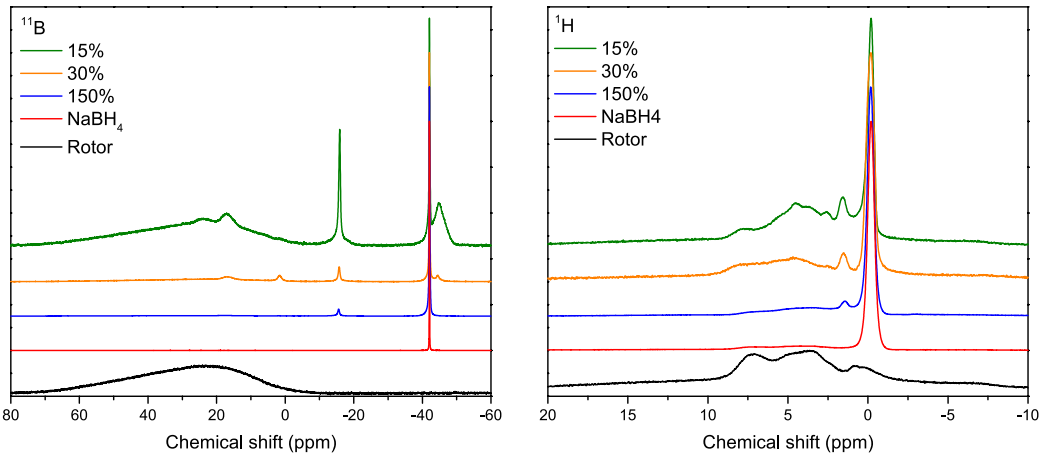

(A) (B)

FIGURE 3.20: High-resolution (A) ^{11}B and (B) ^{1}H NMR spectra of $NaBH_4$@Al_2O_3 composites obtained at 60kHz MAS.

present. To obtain the spin-lattice relaxation time of the broad feature, the inversion recovery method is applied to the 5% composite. This is performed at 283K, 303K and 323K, where the spectra for 303K are shown in Figure 3.19b. From this method, spin-lattice spin-lattice relaxation times are found to be $T_1 = 20.59ms, 9.90ms$ and $5.13ms$ at 273K, 313K and 353K respectively. These are much shorter spin-lattice spin-lattice relaxation times than the sharp feature, roughly determined in the 15% sample. Although clear temperature dependence is observed, more measured temperatures, broader temperature range or magnetic field strengths should be used for an Arrhenius type activation energy determination, with solid-state NMR.[88]

To further investigate the interfacial effects in $NaBH_4$@Al_2O_3 composites, high-resolution solid-state NMR measurements are performed on pure $NaBH_4$, 150%, 30% and 15% $NaBH_4$@Al_2O_3 composites and an empty rotor. All spectra are obtained at 60kHz MAS. The $NaBH_4$ containing spectra are normalized to the single present peak in pristine $NaBH_4$ (-0.2ppm for ^{1}H and -42.0ppm for ^{11}B). Rotor spectra are normalized by the same factor as the 15% sample for comparison of any rotor and/or probe background signals.

In Figure 3.20a the ^{11}B spectra are depicted. For pure $NaBH_4$ a single peak is observed at -42.0ppm, which is also visible in all composite spectra. This peak is ascribed to bulk-like $[BH_4]^-$ species. Slightly upfield, at lower chemical shift, a second peak arises for lower pore fillings at -44.8ppm. Because of the similar chemical shift, this is ascribed to a slightly more shielded $[BH_4]^-$ species. In the case of $LiBH_4$, similar results are found, where nanoclusters of $(LiBH_4)_N$, with $N = 3 - 5$ showed slightly more shielding of the boron, compared to the bulk.[89] Here, the peak at -44.8ppm is therefore ascribed to nanoclusters of $NaBH_4$ in the pores.

Three minor contributions are found at chemical shifts of 24.4, 17.4 and 1.3ppm. Following the work of Züchner et al. on sodium aluminoborate glasses, these peaks can be ascribed to species similar to three-coordinate $BO_{2/2}O^-$ species, trigonal $BO_{3/2}$ units and tetragonal $BO^-_{4/2}$ sites respectively.[90]

These findings indicate a chemical environment where boron is coordinated to more than one oxygen. The dried Al_2O_3 is the only oxygen-containing species in this composites starting material, and therefore this indicates chemical bond formation between the support alumina and the borohydride anion. Such support-salt effects have been reported for LiF/Al_2O_3 composites.[86]

Lastly, a sharp arising feature is found at -15.6ppm in the ^{11}B spectrum. This feature is found outside of the region of $[BH_4]^-$ or borohydride-alumina species at the interface. As indicated by DRIFTS, traces of $Na_2B_{12}H_{12}$ are found after melt infiltration. Previous work has shown traces of $Na_2B_{12}H_{12}$ by ^{11}B NMR after melt infiltration around 13ppm.[91] Measurement with a higher resolution determined the ^{11}B signal in $Na_2B_{12}H_{12}$ to be at ∼-15.5ppm, matching the findings of this work.[92] Note that this $Na_2B_{12}H_{12}$ was not observed with XRD, at either low or high pore filling (see Figure A.3), and is therefore ascribed as an amorphous species within the composite

Although from Figure 3.20a the $Na_2B_{12}H_{12}$ signal appears more prominent at lower pore filling samples, the non-normalized intensities are similar in all composite spectra (Figure A.8). Therefore, a similar amount of $Na_2B_{12}H_{12}$ is formed at different pore fillings, and bulk-like features decrease in intensity. It is suggested this $Na_2B_{12}H_{12}$ formation occurs at the interface of the alumina, as every composite contains a similar amount of alumina surface area. The relative amount of $Na_2B_{12}H_{12}$ in $NaBH_4@Al_2O_3$ composites that are measured with EIS (>100% pore filling) is small compared to $NaBH_4$. However, the high ionic conductivity of $Na_2B_{12}H_{12}$ and $Na_3BH_4B_{12}H_{12}$ could give rise to the overall enhanced conductivity of the composite.[25,33]

Furthermore, it was found that $[B_{12}H_{12}]^{2-}$ has a fast spin-lattice relaxation time in the millisecond time regime compared to slower second time regime of the $[BH_4]^-$ and the borate species (see Figure A.9a). This fast relaxation time is in line with the literature on $Na_2B_{12}H_{12}$.[93] High-resolution ^{23}Na NMR spectra show a shoulder arising in the composites slightly upfield compared to pristine $NaBH_4$ (see Figure A.9b). This contribution is not accurately determined and could arise from for example $Na_2B_{12}H_{12}$ species or sodium in close proximity the alumina surface.

In Figure 3.20b the high-resolution ^1H spectra are depicted. For pure $NaBH_4$ a single peak is observed at -0.2 ppm, which is also visible in all composite spectra. The composites show a peak with higher relative intensity at lower pore fillings, around 1.5ppm. In this region, a peak is found for $CaB_{12}H_{12}$.[92] Although varying the cation could induce a difference in chemical shift, the ^{11}B spectra of $CaB_{12}H_{12}$ and $Na_2B_{12}H_{12}$ are very similar and therefore the 1.5ppm peak could represent the signal from the $[B_{12}H_{12}]^{2-}$ anion.[92] A broad feature around 5ppm seems to be present in the composites, in addition to the signal from the rotor. This peak is not accurately determined, but its chemical shift hints towards O-H species, that could arise from the alumina surface.[94]

This NMR analysis indicates the interfacial effects in $NaBH_4@Al_2O_3$ composites. B-O bonds, $Na_2B_{12}H_{12}$ species and $(NaBH_4)_N$ clusters are suggested to form at the interface, resulting in a mobile, Na-ion that is believed to be the cause of the overall conductivity enhancement.

Chapter 4

Summary and conclusions

In this thesis, several sodium-based complex salts were investigated as potential solid-state sodium-ion-conductors. Interface-engineered nanocomposites of low melting temperature sodium-salts and mesoporous Al_2O_3 and SiO_2 (MCM-41) scaffolds were prepared via melt infiltration. The conductivity of these materials was tested and the interfacial effects were investigated.

From the structural characterisation by XRD was found that confinement in the porous supports induces a loss of long-range crystallinity in $NaBH_4$- and $NaNH_2$-oxide composites. Vibrational spectroscopy has shown a reaction between the sodium salts and support surface hydroxyl groups during melt infiltration. Further investigation on the $NaBH_4$-oxide interface has shown an indication of the formation of $Na_2B_{12}H_{12}$ species and B-O bonds, corresponding to interfacial effects in these composites.

More insight into interfacial effects in $NaBH_4@Al_2O_3$ composites was obtained with solid-state NMR. This has shown a shorter ^{23}Na spin-lattice relaxation time in close proximity to the support interface compared to bulk-like features, possibly due to a higher mobility of Na-ions in the composite. High-resolution solid-state ^{11}B NMR has confirmed the formation of B-O bonds and $Na_2B_{12}H_{12}$ species at the interface, substantiating the observed interfacial effects between $NaBH_4$ and Al_2O_3.

Conductivity measurements of the composites with EIS have shown an enhancement compared to the pristine starting materials. The obtained conductivity at 297K was 2.7×10^{-6} and 3.1×10^{-7} Scm^{-1} for $NaBH_4@Al_2O_3$ and $NaNH_2$@MCM-41 with 130% pore filling, respectively. This is over a thousandfold enhancement compared to pure $NaBH_4$ and $NaNH_2$. From the temperature-dependent Arrhenius behavior, activation energies for sodium hopping of these composites were found to be 0.46 and 0.69 eV respectively, compared to 0.64 and 1.36 eV for the pure $NaBH_4$ and $NaNH_2$. The conductive performance of these composites exceed previously reported metal hydride solid-state sodium-conductors such as Na_3AlH_6 and $Na_2BH_4NH_2$.[30,31]

From this work, the approach of melt-infiltration is shown as a facile and effective synthesis technique for promising novel interface-engineered solid-state sodium-ion conductors for potential applications in all-solid-state sodium-batteries.

Chapter 5

Outlook

As a follow up of the work performed in this thesis some future experiments are proposed. A few examples of additional measurements and ideas are proposed below.

During the melt infiltration of $NaNH_2$ in this work, some uncertainties about its structure after synthesis have arisen. Since $NaNH_2$@MCM-41 shows excellent conductivity, and almost no diffraction intensity, more detailed investigation into the structure of this material would be interesting. In-situ XRD could provide more insight into the loss of crystallinity upon heating. If this loss of crystallinity is initiated by partial decomposition, thermal gravimetric analysis (TGA) could provide useful information. If upon heating any release of ammonia is observed, that could indicate the formation of for example the proposed $Na_3(NH_2)(NH)$ compound.[51] Similarly, DSC measurements under ammonia pressure could be performed to investigate such loss of crystallinity or decomposition from the melting enthalpies.

This work showed preliminary results on the temperature dependence of ^{23}Na relaxation rates in $NaBH_4$@Al_2O_3 in close proximity to the alumina support. To couple these relaxation rates to an activation energy for sodium-ion hopping, relaxation times over broader temperature range, with more data points, or with more than one field strength should be performed. Furthermore, this NMR investigation approach for relaxation time measurements as well as investigation of interfacial effects can be extended to the conductive $NaNH_2$@MCM-41 system.

All conductivity measurements in this thesis were performed with alternating current potentials. Direct current measurements could be performed in a symmetrical cell, comparing between non-blocking (sodium) and blocking (e.g. molybdenum, gold) electrodes. From this, transport number measurements can be obtained and the distinction between electronic and ionic conductivity can be made, which is required to prove the true ionic conductive behavior of these materials.

A model system of similar pore sizes with different surface groups could give more insight into the origin of the effect on the conductivity enhancement by interfacial engineering. Therefore, a retry of the aluminated SBA-15 model system, as described in section 3.2.4, could be very useful for a fundamental understanding of the properties of the support.

Boron-oxygen species were found by NMR for $NaBH_4$@Al_2O_3 and by NEXAFS analysis in the $LiBH_4$-Al_2O_3 system.[37] Therefore, similar synchrotron X-ray techniques such as NEXAFS or resonant inelastic X-ray scattering (RIXS)

could provide insight into the creation of bond at the oxide-metal hydride interface for $NaBH_4@Al_2O_3$ and $NaNH_2$@MCM-41.

Partial anion substitution is a broadly applied approach for enhancement of ionic conductivities. In future work, melt infiltration could be used in a combined approach with partial anion substitution, as an investigation of both of these ionic conductivity enhancement techniques. The complex mixture $Na_2BH_4NH_2$ shows already high ionic conductivity at ambient temperature, which may be further enhanced by melt infiltration in this combined approach.

The most conductive materials found in this work, $NaBH_4@Al_2O_3$ and $NaNH_2$@MCM-41, could be assembled in an all-solid-state battery such as a Na-S battery. The assembled battery can be tested to evaluate the electrochemical stability in the presence of anode and cathode materials.

Acknowledgements

After the past year working on this project, I would like to thank a lot of people who've I've worked with or alongside. Firstly, thanks to dr. Peter Ngene as the initiator of this project. You are thanked for being my daily supervisor, for teaching me the whereabouts of the lab and for all your feedback on presentations, academic posters and this thesis.

I thank dr. prof. Petra de Jongh for the opportunity to do this research in the group of Inorganic Chemistry and Catalysis. Thanks for all fruitful research-related discussions. Thank you for the close involvement and discussions about other research projects regarding internships and PhDs.

Justine Harmel is gratefully acknowledged for providing the Al-SBA-15 samples used in this work. Roman Zettl is acknowledged for the SEM measurements. Remco Dalebout, Sander Lambregts, Miguel Rivera Torrente, Silvia Zanoni and Nikos Nikolopoulos are acknowledged for physisorption measurements.

Prof. dr. Marc Baldus is acknowledged for providing measurement time in the solid-state NMR facility. Thanks to ing. Johan van der Zwan and dr. Andrei Gurinov for performing the measurements on the 400MHz and 950MHz spectrometers respectively.

Thanks to my fellow colleagues of the battery team including PhD candidates and master students for creating a cooperative working environment at the lab and their useful insights and discussions. Being one of the few people working on batteries in this group, was a very pleasant experience with all of you. Thanks to Sander Lambregts and Laura de Kort in particular for all enlightening discussions about the research.

Thanks to my fellow master students from the ICC group during my stay for the alternation between science and general nonsense during coffee breaks and lunches.

Last but not least, thanks to the entire research group for creating an enjoyable workplace including the organization many sociable borrels, dinners and days-out.

Appendix A

Supporting information

ID	Sample description	Support (g)	Salt (g)	comments
MCM	SiO_2			0.837151 cm^3g^{-1}
MCM 06	SiO_2			1.110039 cm^3g^{-1}
MCM 10	SiO_2			1.284407 cm^3g^{-1}
Ox070	Al_2O_3			0.485791 cm^3g^{-1}
OxNew	Al_2O_3			0.457012 cm^3g^{-1}
OBC001	$NaBH_4@Al_2O_3$	1.0	1.1	Solution impregnation
OBC002	$NaBH_4@Al_2O_3$	0.8	1.2	
OBC003	$NaBH_4$@MCM-41	0.4	0.65	
OBC004	$NaBH_4@Al_2O_3$	1.0040	0.6808	
OBC005	$NaBH_4$@MCM-41	0.5060	0.6439	
OBC006	$NaNH_2$@MCM-41	0.4006	0.6061	
OBC007	$NaBH_4$	-	-	heated to 525°C
OBC008	$NaBH_4@Al_2O_3$	1.0058	0.6766	
OBC009	$NaBH_4$@MCM-41	0.5030	0.5833	
OBC010	$NaNH_2@Al_2O_3$	0.3995	0.3543	
OBC011	$NaNH_2$	-	-	heated to 225°C
OBC012	$NaNH_2@Al_2O_3$	0.2917	0.2564	
OBC013	$NaNH_2$@MCM-41	0.1963	0.3884	[1]
OBC014	$NaNO_2@Al_2O_3$	0.5131	0.7134	
OBC015	$NaNO_2$@MCM-41	0.3032	0.9623	
OBC016	$NaClO_3@Al_2O_3$	0.7000	1.1044	
OBC017	$NaClO_3$@MCM-41	0.3089	1.1439	
OBC018	$NaNO_3@Al_2O_3$	1.0931	1.5088	
OBC019	$NaNO_3$@MCM-41	0.2995	1.3029	
OBC020	$NaClO_3@Al_2O_3$	0.7007	1.1064	5 bar O_2
OBC021	$NaClO_3$@MCM-41	0.3936	1.4414	5 bar O_2
OBC022	$NaNO_3@Al_2O_3$	0.9948	1.4115	stainless steel reactor
OBC023	$NaNO_3$@MCM-41	0.4944	1.6300	stainless steel reactor
OBC024	$NaNH_2$	-	-	24h@RT, 8 bar NH_3
OBC025	$NaNH_2$	-	-	4h@150°C, 8 bar NH_3

TABLE A.1: Overview (1/2) of samples prepared in this thesis project. [1] New batch of SiO_2 (MCM 06) for this and all following samples.

ID	Sample description	Support (g)	Salt (g)	comments
OBC026	$NaBH_4$@Al_2O_3 90%	1.4042	0.6544	[2]
OBC027	$NaBH_4$@Al_2O_3 110%	1.3055	0.7439	
OBC028	$NaBH_4$@Al_2O_3 150%	1.15	0.8982	
OBC029	$NaBH_4$@MCM-41 90%	0.5025	0.5387	
OBC030	$NaBH_4$@MCM-41 110%	0.4477	0.5880	
OBC031	$NaBH_4$@MCM-41 150%	0.3909	0.6703	
OBC032	$NaNH_2$	-	-	2h@150°C, 1 bar Ar
OBC033	$NaNH_2$	-		2h@150°C, 8 bar NH_3
OBC034	$NaNH_2$	-	-	2h@150°C, 10 bar H_2
OBC035	$NaBH_4$@Al_2O_3 50%	1.0044	0.2618	
OBC036	$NaBH_4$@MCM-41 50%	0.3463	0.2069	
OBC037	$NaBH_4$@Al_2O_3 170%	1.0024	0.8834	
OBC038	$NaBH_4$@MCM-41 170%	0.3015	0.7083	
OBC039	$NaBH_4$@Al_2O_3 30%	1.0163	0.1588	
OBC040	$NaBH_4$@Al_2O_3 15%	1.5071	0.1169	[3]
OBC041	$NaBH_4$@Al_2O_3 120%	0.4911	0.2941	
OBC042	$NaBH_4$@Al_2O_3 125%	0.5050	0.3062	
OBC043	$NaBH_4$@Al_2O_3 130%	0.5003	0.3169	
OBC044	$NaBH_4$@Al_2O_3 135%	0.5027	0.3311	
OBC045	$NaBH_4$@Al_2O_3 145%	0.502	0.3560	
OBC046	$NaBH_4$@Al_2O_3 70%	0.7009	0.2404	
OBC047	$NaBH_4$@Al_2O_3 200%	0.4999	0.4888	
OBC048	$NaBH_4$	-	-	heated to 525°C
OBC049	$NaBH_4$@SBA-15	0.1426	0.3783	Brown powder
OBC050	$NaBH_4$@Al-SBA-15(20)	0.1162	0.2586	Brown powder
OBC051	$NaBH_4$@Al-SBA-15(10)	0.1505	0.2096	
OBC052	$NaBH_4$@MCM-41 130%	0.1973	0.3543	[4]
OBC053	$NaBH_4$@Al_2O_3 5%	1.4995	0.0367	
OBC054	$NaBH_4$@Al_2O_3 10%	1.4985	0.0746	
OBC055	$NaBH_4$@Al_2O_3 130%	1.0010	0.6353	
OBC056	$NaBH_4$@MCM-41 130%	0.4965	0.8939	
OBC057	$NaNH_2$@Al_2O_3 130%	0.7993	0.6615	
OBC058	$NaNH_2$@MCM-41 130%	0.3995	0.9190	
OBC059	$NaAlCl_4$@Al_2O_3	0.5017	0.5845	
OBC060	$NaAlCl_4$@MCM-41	0.2473	0.8380	

TABLE A.2: Overview (2/2) of samples prepared in this thesis project. New batch of [2] $NaBH_4$ and $NaNH_2$, [3] Al_2O_3 (OxNew) and [4] SiO_2 (MCM 10) for this and all following samples.

FIGURE A.1: Photographic image of stainless steel reactors used for air-tight melt-infiltration of $NaBH_4$ under H_2 pressure.

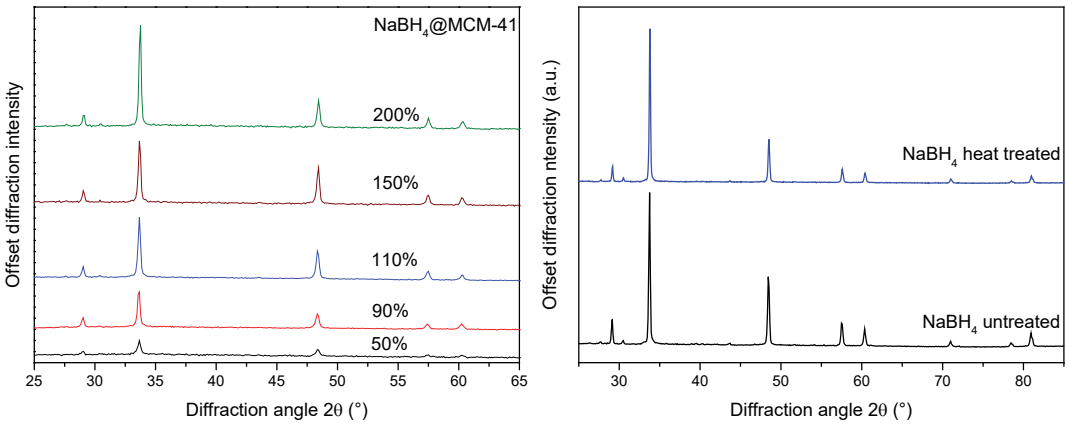

(A) (B)

FIGURE A.2: (A) XRD pattern of $NaBH_4$@MCM-41 with different pore fillings. Little to no loss of long-order crystallinity is observed. (B) XRD pattern of $NaBH_4$ untreated and exposed to the composite treatment (∼5 bar hydrogen to 525°C).

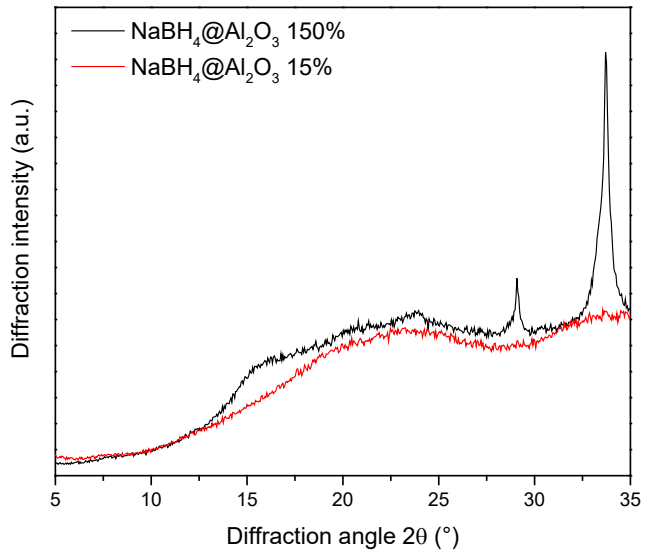

FIGURE A.3: XRD pattern of $NaBH_4@Al_2O_3$ 15% and $NaBH_4@Al_2O_3$ 150%. No crystallinity is observed in the 15% samples, where for 150% only $NaBH_4$ diffraction peaks are found. In both samples, no crystalline $Na_2B_{12}H_{12}$ is observed.

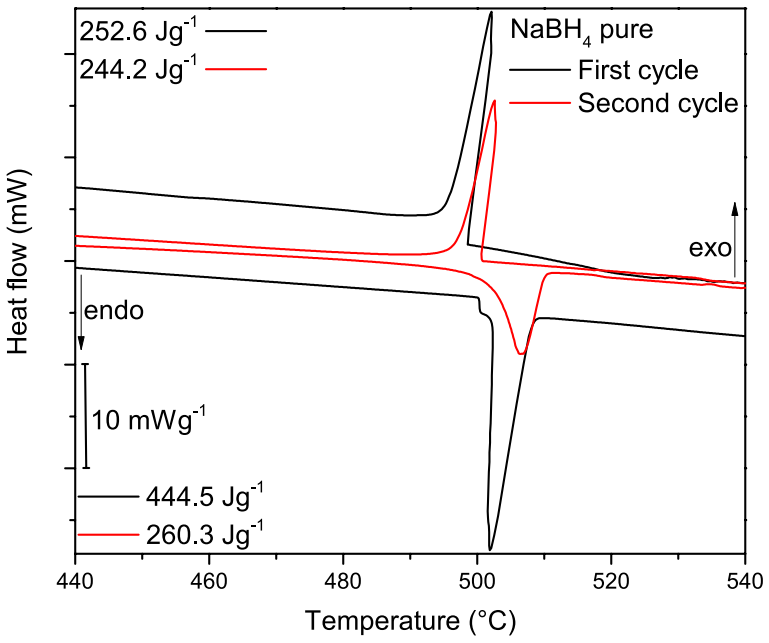

FIGURE A.4: DSC curves of pure $NaBH_4$ cycled between 30 and 550°C with a 10°Cmin^{-1} ramp in the depicted temperature region. Insets indicate the area of the peaks (enthalpy).

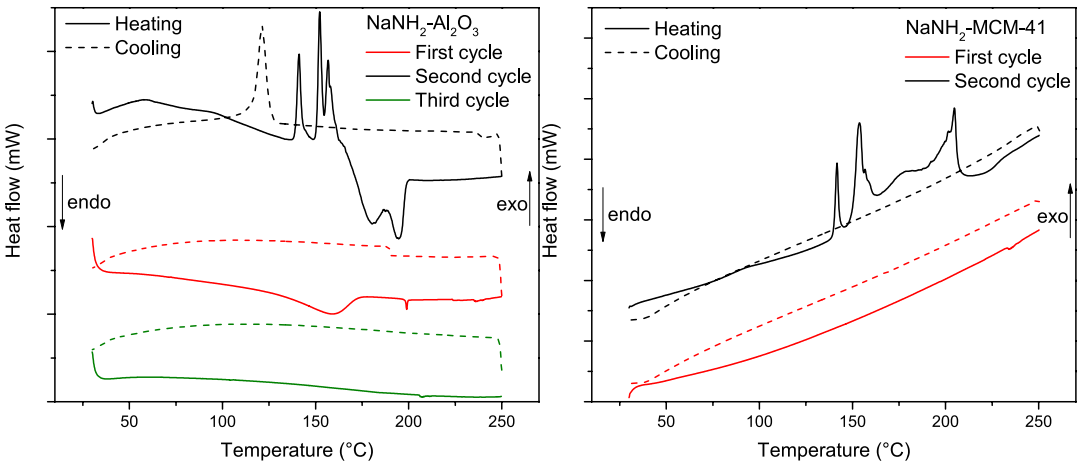

(A) (B)

FIGURE A.5: DSC curves of (A) $NaNH_2$-Al_2O_3 and (B) $NaNH_2$-MCM-41 physical mixtures with a 10°Cmin^{-1} ramp show exothermic decomposition upon heating.

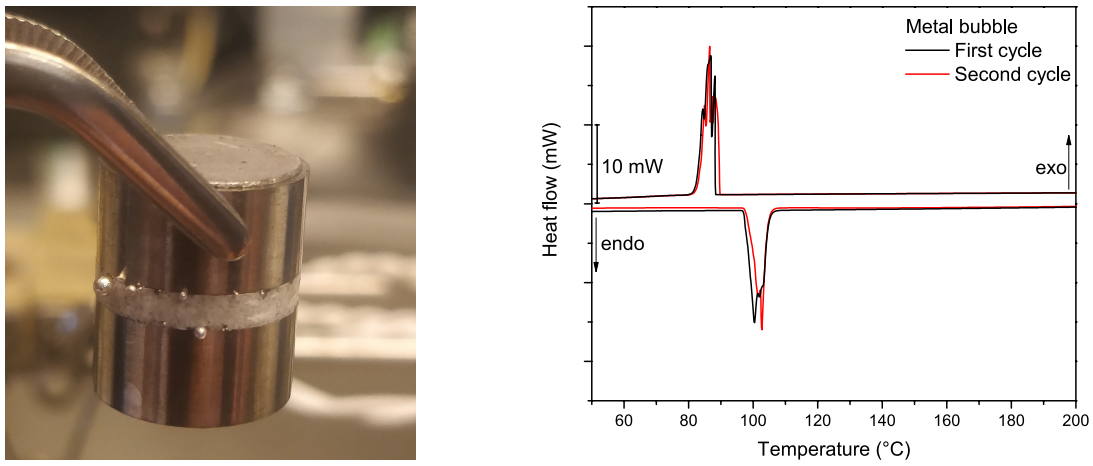

(A) (B)

FIGURE A.6: (A) Photographic image of metallic bubbles after EIS measurement of $NaNH_2$ with Li foil electrodes. (B) DSC curve of the metallic bubbles indicating the formation of metallic sodium (T_m=98.8°C).

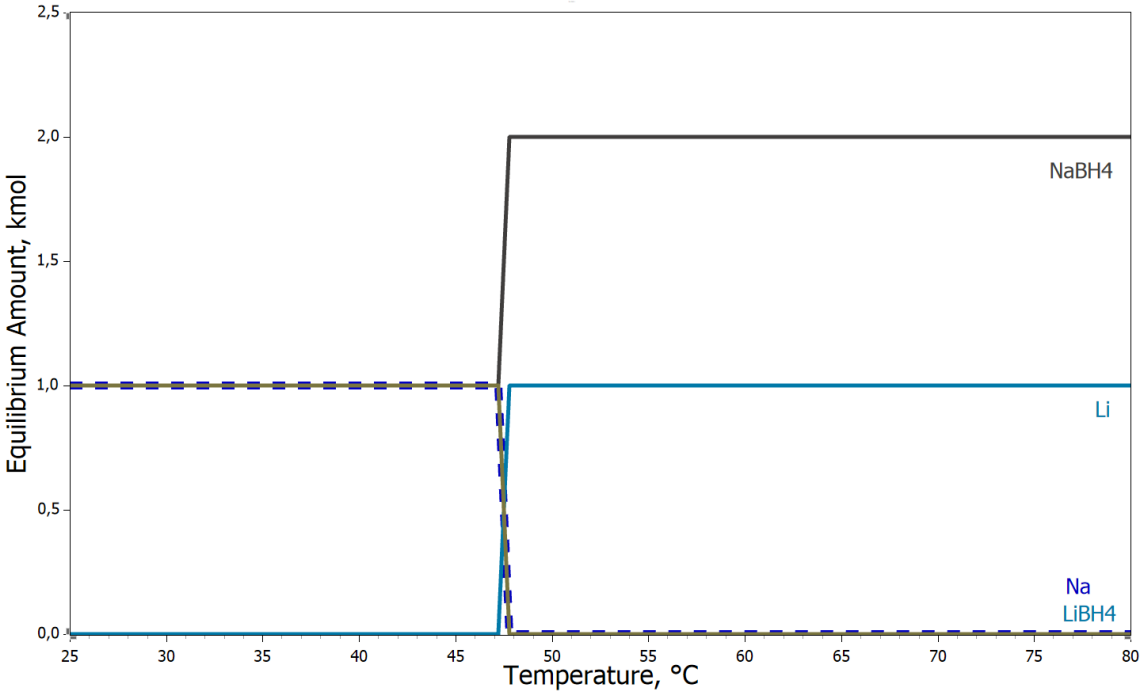

FIGURE A.7: Equilibrium composition of Na, Li, $NaBH_4$ and $LiBH_4$ with 2:1 $NaBH_4$:Li starting material. Calculations performed with HSC Chemistry ® 9.0, Outotec, Pori 2018.

Sample	σ_{RT} (Scm^{-1})	E_{act} (eV)	$NaBH_4$ @Al_2O_3	σ_{RT} (Scm^{-1})	E_{act} (eV)
$NaBH_4$@Al_2O_3	2.73×10^{-6}	0.46	50%	$2.94\times10^{-9*}$	0.59
$NaBH_4$@MCM-41	3.69×10^{-8}	0.49	70%	$4.71\times10^{-7*}$	0.47
$NaBH_4$	$1.30\times10^{-9*}$	0.64	90%	$1.56\times10^{-7*}$	0.52
$NaNH_2$@MCM-41	3.07×10^{-7}	0.69	90%	$2.77\times10^{-7*}$	0.55
$NaNH_2$@Al_2O_3	$8.21\times10^{-9*}$	0.82	90%	$2.11\times10^{-7*}$	0.54
$NaNH_2$ heat treated	$5.85\times10^{-9*}$	0.80	110%	$4.23\times10^{-7*}$	0.56
$NaNH_2$	1.92×10^{-11}	1.36	110%	$3.67\times10^{-7*}$	0.54
$NaBH_4$@SBA	4.18×10^{-8}	0.55	120%	$1.33\times10^{-6*}$	0.49
$NaBH_4$@SBA(20)	2.46×10^{-8}	0.50	125%	$5.11\times10^{-7*}$	0.54
$NaBH_4$@SBA(10)	9.53×10^{-8}	0.54	130%	$1.42\times10^{-6*}$	0.46
$NaBH_4$ heat treated	2.64×10^{-9}	0.72	135%	$3.53\times10^{-7*}$	0.49
$NaNO_2$@Al_2O_3	3.53×10^{-9}	0.90	150%	$7.19\times10^{-7*}$	0.46
$NaNO_2$@MCM-41	$6.70\times10^{-11*}$	1.12	150%	$7.58\times10^{-7*}$	0.51
$NaNO_3$@Al_2O_3	$8.81\times10^{-10*}$	0.92	170%	$6.25\times10^{-7*}$	0.47
90% $NaBH_4$@MCM-41	2.62×10^{-8}	0.52	200%	$8.23\times10^{-7*}$	0.45
130% $NaBH_4$@MCM-41	9.53×10^{-8}	0.45	200%	$7.19\times10^{-7*}$	0.46
150% $NaBH_4$@MCM-41	2.89×10^{-8}	0.50	280%	2.08×10^{-7}	0.50

TABLE A.3: Overview of room temperature conductivity measurements and calculated activation energies obtained by EIS for relevant samples in this thesis. Values with an asterisk are calculated at 25°C from the Arrhenius fit.

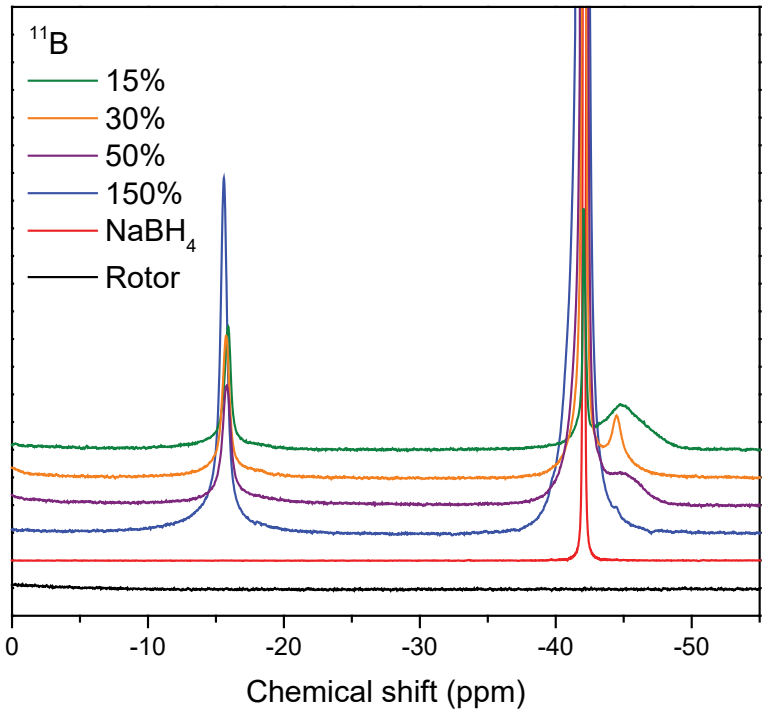

FIGURE A.8: High-resolution non-normalized ^{11}B NMR spectra of $NaBH_4@Al_2O_3$ composites obtained at 60kHz MAS showing the intensity of $Na_2B_{12}H_{12}$ at -15.6ppm is similar for different composites.

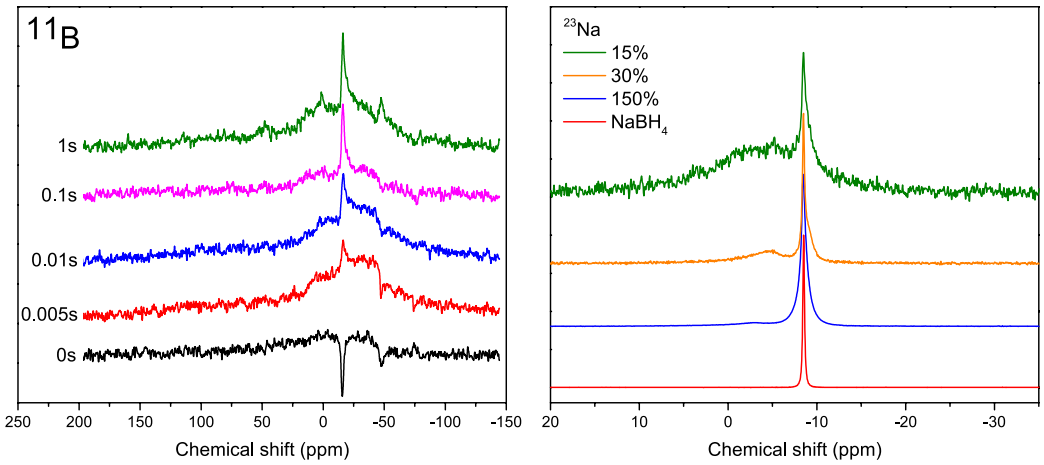

(A) (B)

FIGURE A.9: (A) Inverse recovery method for ^{11}B in $NaBH_4@Al_2O_3$ 5% shows fast relaxation of $Na_2B_{12}H_{12}$ at -15.6ppm. (B) High-resolution NMR ^{23}Na spectra of $NaBH_4@Al_2O_3$ composites obtained at 60kHz MAS.

Bibliography

(1) BP *Statistical review of World Energy*; tech. rep.; 2018.

(2) UN Framework Convention on Climate Change *Adoption of the Paris Agreement*; tech. rep.; 2015.

(3) European Council *2030 Climate and energy policy framework*; tech. rep.; 2014.

(4) Goodenough, J. B.; Park, K. S. *Journal of the American Chemical Society* **2013**, *135*, 1167–1176.

(5) Ozawa, K. *Solid State Ionics* **1994**, *69*, 212–221.

(6) Goodenough, J. B.; Kim, Y. *Journal of Power Sources* **2011**, *196*, 6688–6694.

(7) Mauger, A.; Julien, C. M. *Ionics* **2017**, *23*, 1933–1947.

(8) Yan, Y.; Kühnel, R. S.; Remhof, A.; Duchêne, L.; Reyes, E. C.; Rentsch, D.; Łodziana, Z.; Battaglia, C. *Advanced Energy Materials* **2017**, *7*, 1700294.

(9) Manthiram, A.; Yu, X.; Wang, S. *Nature Reviews Materials* **2017**, *2*, 16103.

(10) Kumar, R.; Liu, J.; Hwang, J. Y.; Sun, Y. K. Recent research trends in Li-S batteries., 2018.

(11) Pan, H.; Hu, Y.-S.; Chen, L. *Energy & Environmental Science* **2013**, *6*, 2338.

(12) Zu, C. X.; Li, H. *Energy and Environmental Science* **2011**, *4*, 2614–2624.

(13) Ellis, B. L.; Nazar, L. F. *Current Opinion in Solid State and Materials Science* **2012**, *16*, 168–177.

(14) Guin, M.; Tietz, F. *Journal of Power Sources* **2015**, *273*, 1056–1064.

(15) Adelhelm, P.; Hartmann, P.; Bender, C. L.; Busche, M.; Eufinger, C.; Janek, J. *Beilstein Journal of Nanotechnology* **2015**, *6*, 1016–1055.

(16) Slater, M. D.; Kim, D.; Lee, E.; Johnson, C. S. *Advanced Functional Materials* **2013**, *23*, 947–958.

(17) Dahbi, M.; Yabuuchi, N.; Kubota, K.; Tokiwa, K.; Komaba, S. *Physical Chemistry Chemical Physics* **2014**, *16*, 15007–15028.

(18) Vaalma, C.; Buchholz, D.; Weil, M.; Passerini, S. A cost and resource analysis of sodium-ion batteries., 2018.

(19) Dunn, B.; Kamath, H.; Tarascon, J. M. *Science* **2011**, *334*, 928–935.

(20) Longo, S.; Antonucci, V.; Cellura, M.; Ferraro, M. *Journal of Cleaner Production* **2014**, *85*, 337–346.

(21) Stanley Whittingham, M.; Huggins, R. A. *The Journal of Chemical Physics* **1971**, *54*, 45–51.

(22) Zhou, W.; Li, Y.; Xin, S.; Goodenough, J. B. *ACS Central Science* **2017**, *3*, 52–57.

(23) Goodenough, J.; Hong, H.-P.; Kafalas, J. *Materials Research Bulletin* **1976**, *11*, 203–220.

(24) Anantharamulu, N.; Koteswara Rao, K.; Rambabu, G.; Vijaya Kumar, B.; Radha, V.; Vithal, M. *Journal of Materials Science* **2011**, *46*, 2821–2837.

(25) Udovic, T. J.; Matsuo, M.; Unemoto, A.; Verdal, N.; Stavila, V.; Skripov, A. V.; Rush, J. J.; Takamura, H.; Orimo, S. I. *Chemical Communications* **2014**, *50*, 3750–3752.

(26) Udovic, T. J.; Matsuo, M.; Tang, W. S.; Wu, H.; Stavila, V.; Soloninin, A. V.; Skoryunov, R. V.; Babanova, O. A.; Skripov, A. V.; Rush, J. J.; Unemoto, A.; Takamura, H.; Orimo, S. I. *Advanced Materials* **2014**, *26*, 7622–7626.

(27) Tang, W. S.; Unemoto, A.; Zhou, W.; Stavila, V.; Matsuo, M.; Wu, H.; Orimo, S. I.; Udovic, T. J. *Energy and Environmental Science* **2015**, *8*, 3637–3645.

(28) De Jongh, P. E.; Blanchard, D.; Matsuo, M.; Udovic, T. J.; Orimo, S. *Applied Physics A: Materials Science and Processing* **2016**, *122*, 251.

(29) Cuan, J.; Zhou, Y.; Zhou, T.; Ling, S.; Rui, K.; Guo, Z.; Liu, H. *Advanced Materials* **2018**, *31*, 1803533.

(30) Matsuo, M.; Kuromoto, S.; Sato, T.; Oguchi, H.; Takamura, H.; Orimo, S. I. *Applied Physics Letters* **2012**, *100*, 203904.

(31) Oguchi, H.; Matsuo, M.; Kuromoto, S.; Kuwano, H.; Orimo, S. *Journal of Applied Physics* **2012**, *111*, 036102.

(32) Yoshida, K.; Sato, T.; Unemoto, A.; Matsuo, M.; Ikeshoji, T.; Udovic, T. J.; Orimo, S. i. *Applied Physics Letters* **2017**, *110*, 103901.

(33) Sadikin, Y.; Brighi, M.; Schouwink, P.; Černý, R. *Advanced Energy Materials* **2015**, *5*, 1501016.

(34) Blanchard, D.; Nale, A.; Sveinbjörnsson, D.; Eggenhuisen, T. M.; Verkuijlen, M. H.; Suwarno; Vegge, T.; Kentgens, A. P.; De Jongh, P. E. *Advanced Functional Materials* **2015**, *25*, 184–192.

(35) Matsuo, M.; Nakamori, Y.; Orimo, S. I.; Maekawa, H.; Takamura, H. *Applied Physics Letters* **2007**, *91*, 224103.

(36) Choi, Y. S.; Lee, Y. S.; Oh, K. H.; Cho, Y. W. *Physical Chemistry Chemical Physics* **2016**, *18*, 22540–22547.

(37) Choi, Y. S.; Lee, Y.-S.; Choi, D.-J.; Chae, K. H.; Oh, K. H.; Cho, Y. W. *The Journal of Physical Chemistry C* **2017**, *121*, 26209–26215.

(38) Stavila, V.; Dimitrievska, M.; Tang, W. S.; Talin, A. A.; White, J. L.; Varley, J.; Shea, P.; Wood, B. C.; Skripov, A.; Udovic, T. J. *ECS Meeting Abstracts* **2017**, *MA2017-02*, 449.

(39) De Jongh, P. E.; Eggenhuisen, T. M. *Advanced Materials* **2013**, *25*, 6672–6690.

(40) Beck, J. S.; Vartuli, J. C.; Roth, W. J.; Leonowicz, M. E.; Kresge, C. T.; Schmitt, K. D.; Chu, C. T. W.; Olson, D. H.; Sheppard, E. W.; McCullen, S. B.; Higgins, J. B.; Schlenker, J. L. *Journal of the American Chemical Society* **1992**, *114*, 10834–10843.

(41) Zhao, D.; Feng, J.; Huo, Q.; Melosh, N.; Fredrickson, G. H.; Chmelka, B. F.; Stucky, G. D. *Science* **1998**, *279*, 548–552.

(42) Lee, H. I.; Kim, J. H.; Stucky, G. D.; Shi, Y.; Pak, C.; Kim, J. M. *Journal of Materials Chemistry* **2010**, *20*, 8483–8487.

(43) Baca, M.; de la Rochefoucauld, E.; Ambroise, E.; Krafft, J. M.; Hajjar, R.; Man, P. P.; Carrier, X.; Blanchard, J. *Microporous and Mesoporous Materials* **2008**, *110*, 232–241.

(44) Li, G.; Lu, X.; Coyle, C. A.; Kim, J. Y.; Lemmon, J. P.; Sprenkle, V. L.; Yang, Z. *Journal of Power Sources* **2012**, *220*, 193–198.

(45) Cheng, C. F.; Zhou, W.; Park, D. H.; Klinowski, J.; Hargreaves, M.; Gladden, L. F. *Journal of the Chemical Society - Faraday Transactions* **1997**, *93*, 359–363.

(46) Guzmán-Castillo, M. L.; Bokhimi, X; Rodríguez-Hernández, A.; Toledo-Antonio, A; Hernández-Beltrán, F.; Fripiat, J. J. *Journal of Non-Crystalline Solids* **2003**, *329*, 53–56.

(47) Brunauer, S.; Kantro, D. L.; Weise, C. H. *Canadian Journal of Chemistry* **1956**, *34*, 1483–1496.

(48) Digne, M.; Sautet, P.; Raybaud, P.; Euzen, P.; Toulhoat, H. *Journal of Catalysis* **2002**, *211*, 1–5.

(49) Landmesser, H.; Kosslick, H.; Storek, W.; Fricke, R. *Solid State Ionics* **1997**, *101-103*, 271–277.

(50) Vajeeston, P.; Ravindran, P.; Fjellvåg, H. *Journal of Nanoscience and Nanotechnology* **2011**, *11*, 1929–1934.

(51) Jepsen, L. H.; Wang, P.; Wu, G.; Xiong, Z.; Besenbacher, F.; Chen, P.; Jensen, T. R. *Physical Chemistry Chemical Physics* **2016**, *18*, 25257–25264.

(52) Züttel, A.; Wenger, P.; Rentsch, S.; Sudan, P.; Mauron, P.; Emmenegger, C. *Journal of Power Sources* **2003**, *118*, 1–7.

(53) Brunauer, S.; Emmett, P. H.; Teller, E. *Journal of the American Chemical Society* **1938**, *60*, 309–319.

(54) Barrett, E. P.; Joyner, L. G.; Halenda, P. P. *Journal of the American Chemical Society* **1951**, *73*, 373–380.

(55) Kubelka, P; Munk, F; Kubelka, P; others *Z. Tech. Physik* **1931**, *12*, 501–593.

(56) Nobbs, J. H. *Review of Progress in Coloration and Related Topics* **1985**, *15*, 66–75.

(57) Klotz, D., *Characterization and Modeling of Electrochemical Energy Conversion Systems by Impedance Techniques*, 2012.

(58) Jensen, S. R.; Jepsen, L. H.; Skibsted, J.; Jensen, T. R. *Journal of Physical Chemistry C* **2015**, *119*, 27919–27929.

(59) Abrahams, S. C.; Kalnajs, J. *The Journal of Chemical Physics* **1954**, *22*, 434–436.

(60) Filinchuk, Y.; Hagemann, H. *European Journal of Inorganic Chemistry* **2008**, 3127–3133.

(61) Papirer, E.; Burneau, A.; Barres, O.; Vidal, A.; Ligner, G.; Balard, H. *Langmuir* **2005**, *6*, 1389–1395.

(62) Peri, J. B. *The Journal of Physical Chemistry* **1965**, *69*, 211–219.

(63) Harvey, K. B.; McQuaker, N. R. *Canadian Journal of Chemistry* **1971**, *49*, 3272–3281.

(64) Zhang, Y.; Tian, Q. *International Journal of Hydrogen Energy* **2011**, *36*, 9733–9742.

(65) Lu, Z.; Zhu, Q.; Li, H.-W.; Zhang, D.; Fu, Y.; Li, X.; Xiong, W.; Shao, H.; He, L.; Deng, Y.; Zhao, X.; Wu, D.; Lin, H.; Cheng, H. *Inorganica Chimica Acta* **2018**, *474*, 16–21.

(66) Liu, Y.; Giri, S.; Zhou, J.; Jena, P. *Journal of Physical Chemistry C* **2014**, *118*, 28456–28461.

(67) Kamitsos, E. I.; Chryssikos, G. D. *Journal of Molecular Structure* **1991**, *247*, 1–16.

(68) Gautam, C.; Yadav, A. K.; Singh, A. K. *ISRN Ceramics* **2012**, *2012*, 1–17.

(69) Coates, J. In *Encyclopedia of Analytical Chemistry*, 2006, pp 10815–10837.

(70) Milanese, C.; Garroni, S.; Girella, A.; Mulas, G.; Berbenni, V.; Bruni, G.; Suriñach, S.; Baró, M. D.; Marini, A. *Journal of Physical Chemistry C* **2011**, *115*, 3151–3162.

(71) Juza, R.; Weber, H. H.; Opp, K. *ZAAC - Journal of Inorganic and General Chemistry* **1956**, *284*, 73–82.

(72) Zalkin, A.; Templeton, D. H. *Journal of Physical Chemistry* **1956**, *60*, 821–823.

(73) Nibler, J. W.; Pimentel, G. C. *Spectrochimica Acta* **1965**, *21*, 887–882.

(74) Balabinskaya, A. S.; Ivanova, E. N.; Ivanova, M. S.; Kumzerov, Y. A.; Pan'kova, S. V.; Poborchii, V. V.; Romanov, S. G.; Solovyev, V. G.; Khanin, S. D. *Glass Physics and Chemistry* **2005**, *31*, 330–336.

(75) Shafirovich, E.; Zhou, C.; Ekambaram, S.; Varma, A.; Kshirsagar, G.; Ellison, J. E. *Industrial and Engineering Chemistry Research* **2007**, *46*, 3073–3077.

(76) Ghellab, T; Charifi, Z; Baaziz, H; Uğur, Uğur, G; Soyalp, F *Physica Scripta* **2016**, *91*, 045804.

(77) Cañas, J.; Piñero, J.; Lloret, F.; Gutierrez, M.; Pham, T.; Pernot, J.; Araujo, D. *Applied Surface Science* **2018**, *461*, 93–97.

(78) Vella, E.; Messina, F.; Cannas, M.; Boscaino, R. *Physical Review B* **2011**, *83*, 174201.

(79) Mýrdal, J. S. G.; Vegge, T.; Rossmeisl, J. Computational Design and Characterization of New Battery Materials., Ph.D. Thesis, Technical University of Denmark, 2013, p 35.

(80) Muetterties, E. L.; Merrifield, R. E.; Miller, H. C.; Knoth, W. H.; Downing, J. R. *Journal of the American Chemical Society* **1962**, *84*, 2506–2508.

(81) Huggins, R. A., *Energy storage: Fundamentals, materials and applications, second edition*, 2015, p 114.

(82) Perry, D., *Handbook of Inorganic Compounds, Second Edition*; CRC Press: 2011, pp 495,853,858.

(83) Paik, B.; Wolczyk, A. *The Journal of Physical Chemistry C* **2019**, *123*, 1619–1625.

(84) Kaizer, E. B.; Kravchenko, N. G.; Poplavnoi, A. S. *Journal of Structural Chemistry* **2018**, *59*, 1251–1257.

(85) Verkuijlen, M. H.; Ngene, P.; De Kort, D. W.; Barré, C.; Nale, A.; Van Eck, E. R.; Van Bentum, P. J. M.; De Jongh, P. E.; Kentgens, A. P. *Journal of Physical Chemistry C* **2012**, *116*, 22169–22178.

(86) Breuer, S.; Pregartner, V.; Lunghammer, S.; Wilkening, H. M. *Journal of Physical Chemistry C* **2019**, *123*, 5222–5230.

(87) Gupta, R. K.; Ferretti, J. A.; Becker, E. D.; Weiss, G. H. *Journal of Magnetic Resonance* **1980**, *38*, 447–452.

(88) Epp, V.; Wilkening, M. *Physical Review B - Condensed Matter and Materials Physics* **2010**, *82*, 020301.

(89) Łodziana, Z.; Błoński, P.; Yan, Y.; Rentsch, D.; Remhof, A. *Journal of Physical Chemistry C* **2014**, *118*, 6594–6603.

(90) Züchner, L.; Chan, J. C. C.; Müller-Warmuth, W.; Eckert, H. *The Journal of Physical Chemistry B* **1998**, *102*, 4495–4506.

(91) Ngene, P.; Van Den Berg, R.; Verkuijlen, M. H. W.; De Jong, K. P.; De Jongh, P. E. *Energy and Environmental Science* **2011**, *4*, 4108–4115.

(92) Stavila, V.; Her, J.-H.; Zhou, W.; Hwang, S.-J.; Kim, C.; Ottley, L. A. M.; Udovic, T. J. *Journal of Solid State Chemistry* **2010**, *183*, 1133–1140.

(93) Skripov, A. V.; Babanova, O. A.; Soloninin, A. V.; Stavila, V.; Verdal, N.; Udovic, T. J.; Rush, J. J. *Journal of Physical Chemistry C* **2013**, *117*, 25961–25968.

(94) Maciel, G. E.; Piedra, G.; Fitzgerald, J. J.; Dec, S. F.; Dando, N. *Inorganic Chemistry* **2002**, *35*, 3474–3478.